



Unveiling the elastic properties of samarium oxide zinc tellurite-based glasses: Judd-Ofelt intensity parameters through structural, experimental, and theoretical studies

R. A. Tafida^{1,2} · S. Thakur³ · M. Y. Onimisi¹ · S. Garba¹ · S. B. Adamu^{2,4} · I. G. Shitu^{2,4} · I. I. Lakin^{2,5}

Received: 12 January 2024 / Accepted: 25 March 2024 / Published online: 24 April 2024

© The Author(s), under exclusive licence to Springer Science+Business Media, LLC, part of Springer Nature 2024

Abstract

The melt quenching technique was used to prepare zinc tellurite glasses with composition of $[(\text{TeO}_2)_{0.7}(\text{ZnO})_{0.3}]_{1-x}[\text{Sm}_2\text{O}_3]_x$, where x is the molar fraction. The glasses were synthesized at various x values of 0.01, 0.02, 0.03, 0.04, and 0.05. X-ray diffraction patterns depict the absence of distinct absorption peaks, indicating its amorphous nature. The shear and longitudinal velocities of the samples were measured using 5 MHz of frequency at room temperature. Physical properties such as density (ρ), and molar volume (V_m) increases from 5.142 to 5.324 g/cm³ and 27.412 to 27.590 cm³/mol. Variations in ultrasonic velocity, elastic moduli, Debye temperature (θ_D), Softening temperature (T_S) and Poisson's ratio (σ) were discussed and correlated with the composition of the glass samples. Additionally, elastic moduli and Poisson's ratio were compared with the theoretically measured data using the four theoretical elastic models of Makishima and Mackenzie, Rocherulle, Bond compression and Ring Deformation models. The Judd-Ofelt parameters (Ω_2 , Ω_4 and Ω_6) are obtained using Judd-Ofelt theory. To determine the possible applications of the synthesized glasses, the spectroscopic parameters were calculated for each band: radiative transition probabilities [A_{MD}/A_{ED}], branching ratio β_R , spectroscopic quality factor (Ω_4/Ω_6), gain bandwidth ($\Delta\lambda_{\text{eff}} \times \sigma_p$) and the optical gain ($\sigma_p \times \tau$). The obtained higher values of gain bandwidth, optical gain, branching ratio, spectroscopic quality factor (1.550) and the radiative transition probabilities show that the glasses prepared are appropriate for laser applications.

Keywords Sm₂O₃ doped zinc tellurite glasses · Elastic modulus · Ultrasonic velocities · Poisson's ratio and J-O intensity parameters

1 Introduction

Highly potential applications of rare-earth-doped glass systems in the field of photonics have attracted significant interest in recent years (Desirena 2011). Tellurite glasses exhibit promising potential applications in various industries, including electric, optical, and electronic fields. Their advantageous semiconducting properties,

large electrical potential, highly dense network, excellent capability of infrared transmission, large dielectric constant, high refractive index, stability, and low melting points collectively contribute to their exceptional characteristics (Sidek et al. 2007). Currently, there is a growing scientific and technological interest in tellurium oxide (TeO_2)-based glasses due to their unique characteristics of commendable stability in their mechanical and chemical strengths, along with a minimum melting temperature. (Tio et al. 2006). Furthermore, they exhibit significant linear as well as nonlinear refractive indices and demonstrate excellent optical transmission at both visible and infrared wavelengths. (Mohamed et al. 2010). The aforementioned properties position tellurite glasses as promising candidates for the advancement of optical devices (Tafida et al. 2022). Under normal conditions, TeO_2 lacks the capability to form glass independently and requires the presence of modifiers such as alkali or alkaline earth, rare earth or transition metal oxides (Tafida et al. 2020). In this investigation, the choice of Sm^{3+} ($4f^5$) among the RE^{3+} ion series is motivated by its remarkable fluorescence in visible region. Furthermore, it possesses favorable traits that make it particularly well-suited for spectral hole burning studies (Lim et al. 2013). Moreover, the Sm^{3+} ion is highly suitable for the analysis of energy transfer processes, thanks to its relatively high quantum efficiency in the lowest emitting $^4\text{G}_{5/2}$ level and the presence of distinct quenching emission channels. Glasses containing Sm^{3+} ions are also captivating owing to their promising applications in highly-dense optical storage, underwater communications, and color displays, as evidenced by previous research (Lim et al. 2013). In our study, Tafida et al. (2022) discovered that addition of ZnO can effectively cover all interstices within glass system, resulting in structural modifications. ZnO can serve as a glass former, modifier, or both, enabling it to occupy spaces within the glass system.

EL-Mallawany et al. reported, elastic constants provide detailed structural information of solids due to their direct relation with interatomic forces and potentials (El-Mallawany 1998). Ultrasonic longitudinal and shear velocity measurements play a vital role in the investigation of elastic properties in glasses. The ultrasonic velocity can be closely linked to elastic moduli, and changes in these moduli which can provide insights into the structural stability, formation of the glass network, and rigidity. This relationship has been confirmed by previous studies (El-Mallawany 1998). Numerous authors have extensively investigated RE-doped ZnTeO_2 glass systems, and their studies have provided insights into the optical and elastic characteristics of glass systems. The literature contains a significant body of work reporting on these aspects (Usman et al. 2018; Hasnimulyati et al. 2017; Maheshvaran et al. 2011). To our knowledge, there is currently no comprehensive report available on the experimental and theoretical elastic properties of Sm^{3+} doped zinc tellurite glasses analyzed using Judd-Ofelt intensity parameters. Hence, this study represents the synthesis of zinc tellurite glass network incorporated with Sm^{3+} ions, focusing on characterization of their structural properties as well as experimental and various theoretical elastic properties.

The main objectives of the current study are as follows: (i) To synthesize zinc tellurite glasses with Sm^{3+} ions doping. (ii) To investigate the structural properties of glass system. (iii) To examine the influence of samarium oxide concentration on the experimental and theoretical elastic properties of the glasses. (iv) To study the gain bandwidth and optical gain along with branching ratio, and the radiative transitions detected in $^4\text{G}_{5/2} \rightarrow ^6\text{H}_{7/2}$ transition. Thus, suggesting the potential use of fabricated glasses as visible lasers emitting intense orange (604 nm) light in visible region.

2 Experimental procedure

2.1 Sample preparation

Different compositions of Sm_2O_3 were used to dope the zinc tellurite glass system. Glass samples were fabricated by employing the melt quench technique and subjected for characterization. In the present study, the glass samples were synthesized following the specified chemical arrangements. The Sm_2O_3 doped zinc tellurite with chemical composition of $[(\text{TeO}_2)_{0.7} (\text{ZnO})_{0.3}]_{1-x} [\text{Sm}_2\text{O}_3]_x$ were fabricated, where $x=0.01, 0.02, 0.03, 0.04, \text{ and } 0.05$. The necessary ingredients, namely tellurium oxide (TeO_2), zinc oxide (ZnO), and samarium oxide (Sm_2O_3) with a purity of 99.99% from Alfa Aesar, were accurately weighed using weighing balance with a precision of 0.0001 g. The chemical powders were then stirred for approximately 30 min. The preheating and melting processes were made at temperatures of 400 °C and 900 °C, respectively. The molten liquid was rapidly poured into a preheated mold and immediately transferred to the annealing process in the furnace at kept 400 °C for duration of 90 min. The resulting glass samples were carefully sliced to a thickness of 5 mm and underwent meticulous polishing to achieve parallel and transparent surfaces.

2.2 Sample characterization

The density of the samples was measured using an electronic densimeter (MD-300S) based on the principle of Archimedes, with distilled water as the submerging liquid at room temperature. To determine the density of glass system, the following relation was used (Hamza et al. 2019a);

$$\rho_s = \frac{M_a}{V} \quad (1)$$

where, M_a denotes the mass of the sample in air, ρ_s represents the density of the glass sample measured in g/cm^3 , and V represents its corresponding volume measured in grams or cubic centimeters (cm^3). The values of molar volume V_m were computed using relation given in Eq. (2) (Umar et al. 2017);

$$V_m = \sum \frac{X_i M_i}{\rho} \quad (2)$$

where X_i is the molar fraction, M_i represents the molecular weight for i th component, and ρ represents density of the sample. The X'Pert PRO Panalytical Philips instrument was employed to analyze the spectra and validate the amorphous nature of the synthesized glasses. The values of OPD and V_o were computed by employing Eq. (3) (Usman et al. 2018).

$$OPD = n \times \frac{\rho}{M} \times 1000 \quad (3)$$

where n is the number of oxygen's present in sample, ρ is density whereas M is the molecular weight of glass samples.

$$V_o = \frac{V_m}{\sum X_i n_i} \quad (4)$$

where n_i is the number of oxygens in i th component of sample. The values of Sm^{3+} ion concentration (N) and interionic distance (R_i) in glass samples are determined using Eqs. (5) and (6) (Rao et al. 2014).

$$N = \frac{N_A \rho x}{M_w} \quad (5)$$

$$R_i = \left(\frac{1}{N}\right)^{1/3} \quad (6)$$

where N_A , ρ , x , M_w represents the Avogadro's number, glass samples' density, mole fraction of samarium ion and average molecular weight of samples respectively. The measuring unit used for calculating N is (ions/cm³). It is an important parameter used in determining and investigating the interionic forces of samples. The Ritec Ram-5000 Snap Ultrasonic System was employed to estimate the elastic parameters and passage time of the ultrasonic wave in the sample. The determination of ultrasonic velocities data was based on time-interval data (Sidkey and Gaafar 2004).

$$v = \frac{2x}{\Delta t} \quad (7)$$

The measurements of ultrasonic velocities were performed at room temperature using a 5 MHz frequency. In this context, x represents the thickness of the sample, v denotes the ultrasonic velocity, and Δt represents the time difference of flight. Further to ensure accuracy, each measurement was repeated multiple times. The experimentally determined values of longitudinal and shear ultrasonic velocities are denoted as v_l and v_s respectively. The experimental elastic moduli of synthesized samples are determined by employing following relations (Alazoumi et al. 2017);

$$L = v_l^2 \rho \quad (8)$$

$$G = v_s^2 \rho \quad (9)$$

$$K = L - \left(\frac{4}{3}\right)G \quad (10)$$

$$E = (1 + \sigma)2G \quad (11)$$

$$\sigma = \frac{(L - 2G)}{2(L - G)} \quad (12)$$

where G represents shear modulus, v_s is shear velocity, K the bulk modulus and E is Young's modulus whereas σ denotes the Poisson's ratio. L represents the longitudinal modulus, v_l is longitudinal velocity. The theoretical models utilized to describe elastic behavior encompass various models, including bulk compression, the Makishima-Mackenzie model,

and the Rocherulle model. The measurements of elastic moduli are done by using following equations (Sidkey and Gaafar 2004).

$$K_{bc} = \frac{N_A \rho}{9M} \sum_i x_i (n_f)_i r_i^2 f_i \quad (13)$$

$$\sigma_{bc} = 0.28 (\bar{n}_c)^{-1/4} \quad (14)$$

$$G_{bc} = \left(\frac{3}{2}\right) K_{bc} \left(\frac{1 - 2\sigma_{bc}}{1 + \sigma_{bc}}\right) \quad (15)$$

$$L_{bc} = K_{bc} + \left(\frac{4}{3}\right) G_{bc} \quad (16)$$

$$E_{bc} = 2G_{bc} (1 + \sigma_{bc}) \quad (17)$$

where x_i is molar fraction of i th oxide, n_f is number of network bonds per unit glass, r is bond length, f is first order stretching force constant, (\bar{n}_c) is per unit cross-link density and n is coordination number. Additionally, (n_b) is number of bonds per unit volume and to estimate the first order stretching force constant F following equations are being employed (Bootjomchai 2015);

$$n_b = \frac{N_A \rho}{M} \sum_i x_i (n_f)_i \quad (18)$$

$$(\bar{n}_c) = \frac{1}{\eta} \sum_i x_i (n_c)_i (N_c)_i \quad (19)$$

$$f = \frac{1.7}{r^3} \quad (20)$$

where n_c is density of cross-link per unit cation and is equals to (no. of bands-2), N_c is no. of cations per unit glass and η is the total cations present per unit glass. In order to calculate the elastic behaviour of glasses, the theoretical models such as the Makishima and Mackenzie can be employed by using energy dissociation value of oxides per unit volume (G_i) and their packing density (V_i) (Tafida et al. 2023). The equations given below are used to estimate elastic moduli and Poisson's ratio (Hasnimulyati et al. 2017).

$$K_{mm} = 1.2 V_t E_{mm} \quad (21)$$

$$E_{mm} = 83.6 V_t \sum_i G_i X_i \quad (22)$$

where G_t and V_t factor is the summation component expressed as follows;

$$G_t = \sum_i G_i X_i \quad (23)$$

$$V_t = \left(\frac{\rho}{M_w} \right) \sum_i V_i X_i \quad (24)$$

$$G_{mm} = \frac{3E_{mm}K_{mm}}{9K_{mm} - E_{mm}} \quad (25)$$

$$\sigma_{mm} = \frac{E_{mm}}{2G_{mm}} - 1 \quad (26)$$

where symbols used such as G_i and V_i , have meanings that have been previously discussed. In the Rocherulle model, the elastic moduli of a glass sample are known to be affected by both the dissociation energy and their configuration. Experimental investigations have revealed that elastic moduli are not dependent on overall density of the glass sample, but rather on the densities of each oxide present in the glass network. To incorporate these considerations, specific adjustments were made to determine the packing factor of each individual oxide, denoted as C_i , as expressed in the following equation (Zaid et al. 2011).

$$C_i = N_A \cdot \frac{\rho}{M} \cdot \frac{4\pi}{3} \cdot (mR_A^3 + nR_O^3) \quad (27)$$

where m is no. of cations, R_A the ionic radii of cations, n is anions and R_O is ionic radii of the anion in glass network. The remaining equations utilized for calculating the elastic moduli bear resemblance to those found in the Makishima and Mackenzie model. However, there is a notable difference in the determination of the total packing density, C_t , which is assessed independently of the sample density.

$$C_t = \sum_i C_i X_i \quad (28)$$

The following equations can be used to obtain elastic moduli suggested by Rocherulle model;

$$E_{rm} = 2C_t \sum_i G_i X_i \quad (29)$$

$$K_{rm} = 1.2C_t E_{rm} \quad (30)$$

$$G_{rm} = \frac{3E_{rm}K_{rm}}{9K_{rm} - E_{rm}} \quad (31)$$

$$\sigma_{rm} = \frac{E_{rm}}{2G_{rm}} - 1 \quad (32)$$

3 Results and discussion

3.1 Investigation of X-ray diffraction (XRD)

X-ray diffraction (XRD) is a technique for identifying the crystalline phase of a sample material. It is used to analyse the structure of amorphous materials such as glass, as well as to confirm the absence of any crystalline phases (Azlan et al. 2017a). Figure 1 shows the XRD pattern for Sm_2O_3 doped zinc tellurite glass system at different concentrations. A broad diffuse pattern is observed ranging from 20° to 40° at 2θ scale due to the absence of long-range periodic order arrangement in glass structure. Thus, the absence of such sharp diffraction peaks confirm amorphous nature of glass system (Maheshvaran et al. 2012).

3.2 Analysis of density and molar volume

Density is an important physical parameter that reflects the change in glass composition (Hajer et al. 2014). The recorded values of density and molar volume can be found in Table 1, while Fig. 2 illustrates the comparative behavior of these two quantities. It is observed that the density increases as the Sm_2O_3 content increases. The increase in density can be ascribed to the substitution of tellurium oxide, a glass former with a smaller atomic mass ($\text{Te} = 127.6 \text{ g/mol}$), by the dopant samarium, which possesses a larger atomic mass ($\text{Sm} = 150.36 \text{ g/mol}$) within the glass system (Linda et al. 2013). Additionally, the upward trend in density can be attributed to the introduction of a modifier oxide, disrupting the Te-O-Te bonds and consequently expanding the available space within the glass network (Hajer et al. 2016). Moreover, the rise in densities can be ascribed to alterations in coordination and geometrical configuration, as well as structural softening/compactness and changes in the dimensions of interstitial spaces within the glass system (Hajer et al. 2016). The expansion in molar volume within the range of $27.412 \text{ cm}^3/\text{mol}$ to $27.590 \text{ cm}^3/\text{mol}$ can be attributed to the increase of free volume within the glass system (Tafida et al. 2020).

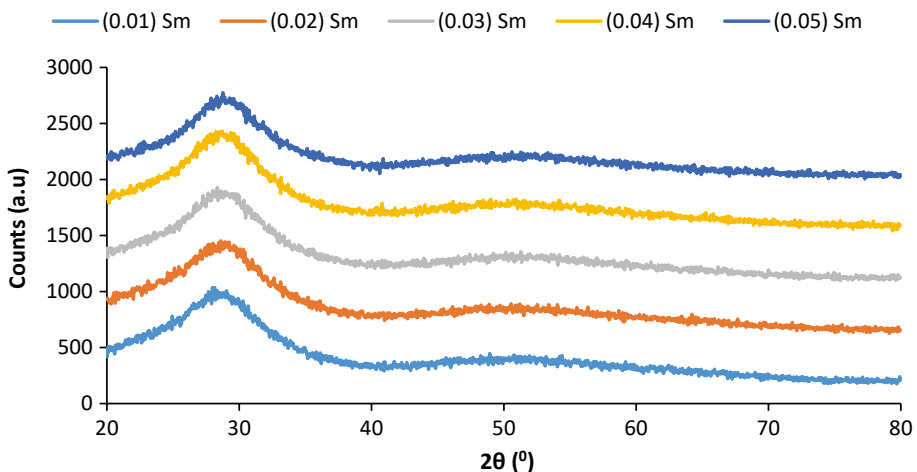
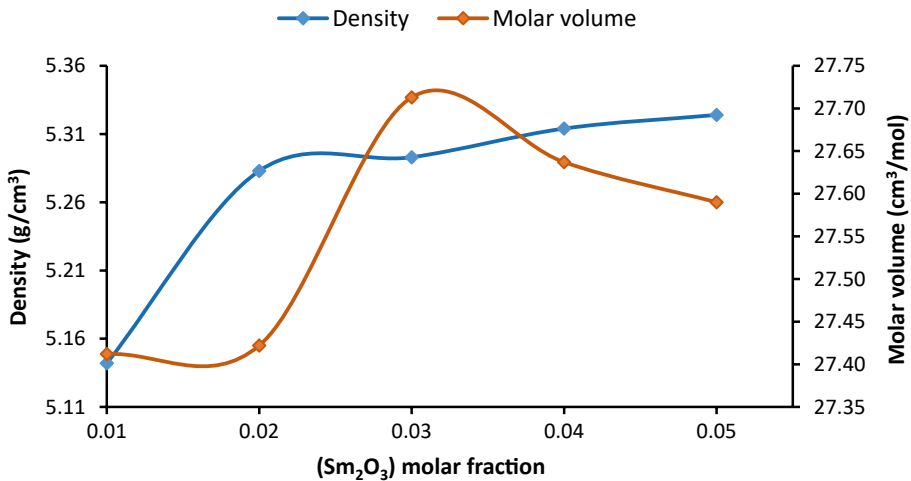


Fig. 1 XRD spectra for $[(\text{TeO}_2)_{0.7}(\text{ZnO})_{0.3}]_{1-x}[\text{Sm}_2\text{O}_3]_x$ glass system

Table 1 Density, molar volume, Oxygen packing density (OPD) and oxygen molar volume (V_o), samarium ionic concentration (N) and inter ionic distance (R_i) for $[(TeO_2)_{0.7}(ZnO)_{0.3}]_{1-x}[Sm_2O_3]_x$ glass system

| Molar fraction (Sm_2O_3) | Density (g/cm^3) [± 0.03] | Molar volume (cm^3/mol) [± 0.05] | OPD (gm-atm/l) | V_o (cm^3/mol) | N ($\times 10^{20}$) | R_i ($\times 10^{-7}$) |
|------------------------------|-------------------------------------|--|----------------|----------------------|------------------------|----------------------------|
| 0.01 | 5.142 | 27.412 | 62.463 | 16.009 | 1.800 | 1.771 |
| 0.02 | 5.283 | 27.422 | 62.616 | 15.970 | 4.245 | 1.330 |
| 0.03 | 5.293 | 27.713 | 62.524 | 15.993 | 6.206 | 1.172 |
| 0.04 | 5.314 | 27.637 | 63.164 | 15.831 | 8.166 | 1.069 |
| 0.05 | 5.324 | 27.590 | 63.741 | 15.688 | 10.211 | 0.993 |

**Fig. 2** Density and molar volume for $[(TeO_2)_{0.7}(ZnO)_{0.3}]_{1-x}[Sm_2O_3]_x$ glass system

The increase can also be attributed to the substitution of smaller atomic/ionic radius atoms (Te and Zn) with larger atomic/ionic radius Sm^{3+} atoms within the glass system.

3.3 Oxygen packing density (OPD) and oxygen molar volume (V_o)

The oxygen packing density and oxygen molar volume serve as indicators of compactness in oxide network (Bhatia et al. 2015). Figure 3 depicts OPD and V_o and their corresponding values are listed in Table 1. The packing density of Sm_2O_3 glasses exhibits a gradual increase as the dopant concentration increases, with values ranging from 62.463 g/litre to 63.741 g/litre. This rise in packing density can be attributed to the increase in glass rigidity and density of the fabricated samples. The presence of Sm^{3+} ions occupying the interstices in the glass network structure leads to a closely packed structure, thereby increasing the glass packing density (Bootjomchai 2015). Furthermore, the increase in packing density can be attributed to the variations in glass network structure around the dopant cations, which result in an increase in their cation field strength. This change in the network configuration contributes to the higher packing density observed in the samples (Abd Elfadeel

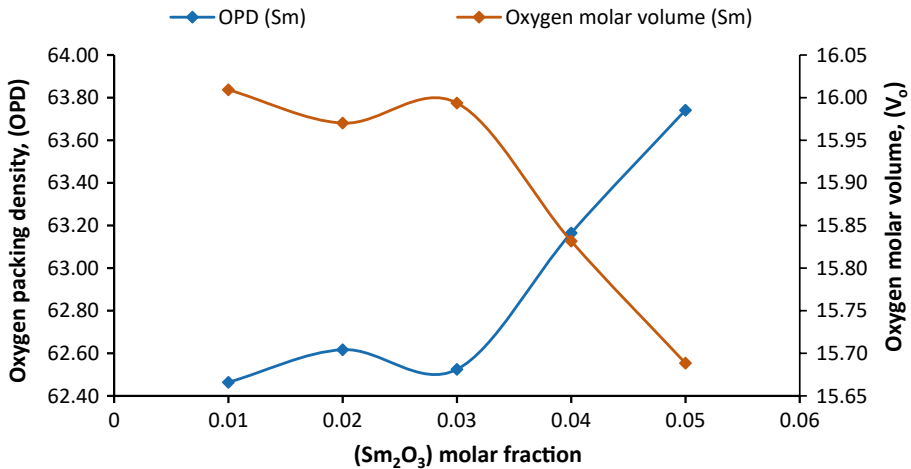


Fig. 3 Oxygen packing density and oxygen molar volume for $[(\text{TeO}_2)_{0.7}(\text{ZnO})_{0.3}]_{1-x}[\text{Sm}_2\text{O}_3]_x$ glass system

et al. 2017). Besides that, the observed rise in OPD implies the absence of non-bridging oxygens (NBOs) in the structure of the glass network (Usman et al. 2018). Nevertheless, the declining values of OPD can be attributed to the presence of NBOs within the glass network. (Ashur et al. 2014). As the dopant content increases, the oxygen molar volume of Sm_2O_3 exhibits a consistent decline. This decrease in oxygen molar volume further contributes to a reduction in the overall molar volume of glass network. It signifies a decrease in the formation of non-bridging oxygen (NBO), consequently leading to a decrease in the available free or excess volume within the glass network. The observed trend favors the formation of a more densely packed structure within the glass network (Gaafar et al. 2014).

3.4 Samarium ionic concentration (N) and inter ionic distance (R_i)

These two factors are crucial in explaining the structural characteristics of tellurite doped glasses. Literature suggests (Hamza et al. 2019a) that as the ionic concentration in the glass system increase, the distance between ions decreases, resulting in a higher level of connectivity within the glass network. The ionic concentration (N) demonstrates an upward trend with the increase of dopant concentration. Conversely, the interionic distance (R_i) decreases with an increase in dopant content, as depicted in Fig. 4, and their respective values are provided in Table 1.

4 Experimental elastic properties

The elastic properties play a crucial role in providing detailed descriptions of the structure of solids. Moreover, they enable the study of material strength under applied forces (Elkhoushkany et al. 2015). Elastic properties are additionally vital parameters utilized to assess the suitability of glasses for various applications (Halimah et al. 2021).

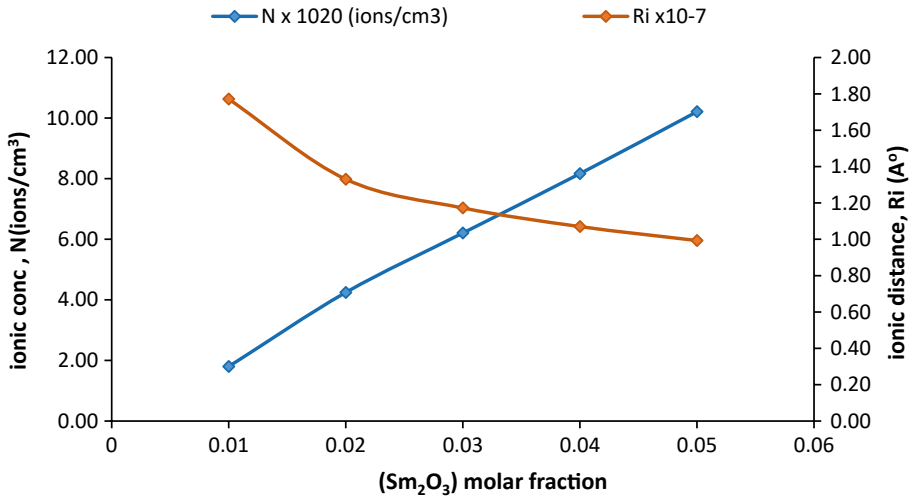


Fig. 4 Ionic concentration and inter ionic distance for [(TeO₂)_{0.7}(ZnO)_{0.3}]_{1-x}[Sm₂O₃]_x glass system

4.1 Longitudinal velocity (V_l) and shear velocity (V_s)

The variation of longitudinal and shear velocity with different dopant concentration is presented in Fig. 5 and their corresponding values are listed in Table 2. Both the longitudinal and shear ultrasonic velocities exhibit similar pattern of behaviour. It is observed that ultrasonic velocities decrease from (3392 to 3379) ms⁻¹ and (1946 to 1920) ms⁻¹ respectively on increasing the dopant content. Nevertheless, when the molar fraction reaches x=0.02, both longitudinal and shear ultrasonic velocities begin to rise until x=0.03. However, from x=0.03 to x=0.05, the velocities start to decline with the increase in dopant. This decrease

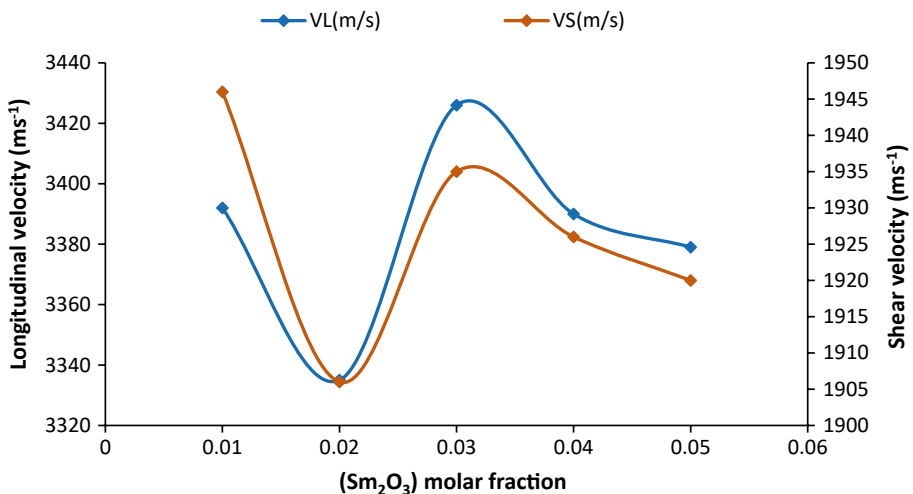


Fig. 5 longitudinal and shear velocities for [(TeO₂)_{0.7}(ZnO)_{0.3}]_{1-x}[Sm₂O₃]_x glass system

Table 2 Longitudinal velocity (V_l), Shear velocity (V_s) and elastic moduli for [(TeO₂)_{0.7} (ZnO)_{0.3}]_{1-x} [Sm₂O₃]_x glass system

| Molar fraction (Sm ₂ O ₃) | V_l (m/s) | V_s (m/s) | L (GPa) | E (GPa) | K (GPa) | G (GPa) |
|--|-------------|-------------|---------|---------|---------|---------|
| 0.01 | 3392 | 1946 | 55.466 | 45.363 | 30.744 | 17.986 |
| 0.02 | 3335 | 1906 | 55.621 | 45.444 | 31.228 | 18.069 |
| 0.03 | 3426 | 1935 | 56.897 | 46.356 | 32.271 | 18.369 |
| 0.04 | 3390 | 1926 | 56.908 | 46.752 | 33.416 | 18.469 |
| 0.05 | 3379 | 1920 | 57.524 | 46.862 | 33.760 | 18.572 |

in longitudinal and shear velocities can be attributed to the formation of NBOs in the glass network (Zaitizila et al. 2018).

On the contrary, the observed increase in value with addition of more dopant can be attributed to the enhanced rigidity of glass system (Nazrin et al. 2018). The increase in rigidity can be linked to the escalation in the quantity of trigonal bipyramid TeO₄ units within the glass network, corresponding to the rise in dopant content (Bahari et al. 2013). Additionally, as given in the literature, an increase in both ultrasonic velocities results in an increase of packing density. This phenomenon arises from the alteration in coordination within the synthesized glasses, leading to the formation of more bridging oxygen (BOs). Consequently, the increase in ultrasonic velocities is directly correlated with this increase in BOs (Saddeek et al. 2005).

4.2 Elastic moduli

The elastic moduli are directly influenced by the interatomic forces and packing density of the constituents oxide (Nazrin et al. 2018). The elastic moduli of the studied glasses were calculated using the measured ultrasonic velocities and density. Table 2 presents the values of the elastic moduli, while Fig. 6 illustrates the variation of the elastic moduli at different dopant concentrations. It is observed that the elastic moduli L, G, K, and E increase with increasing dopant concentrations. This increase is attributed to the enhanced glass rigidity resulting from the addition of more dopants into the glass network (Sidek et al. 2007). Moreover, as the elastic modulus increases with the addition of dopants, it indicates an improvement in the strength of the materials (Alazoumi et al. 2017). With an increase in connectivity, the samples demonstrate a higher level of atom bonding within the glass network, resulting in improved resistance to strain.

4.3 Poisson's ratio (σ) and Fugacity (f_g)

According to the literature, Poisson's ratio present the degree of cross-link density within the glass network (Gupta et al. 2014). This suggests that Poisson's ratio is influenced by the density of cross-links and can be analyzed using cross-link density data. Poisson's ratio is also linked to the internal changes occurring within the glass materials (Abd Elfadeel et al. 2017). The data for Poisson's ratio is listed in Table 3 and presented in Fig. 7. The values of Poisson's ratio increase up to a dopant concentration of 0.03 molar fractions and then decrease until 0.05 molar fractions with the addition of dopant. The increase in Poisson's ratio suggests a higher level of transverse contracting strain among the atoms, resulting in

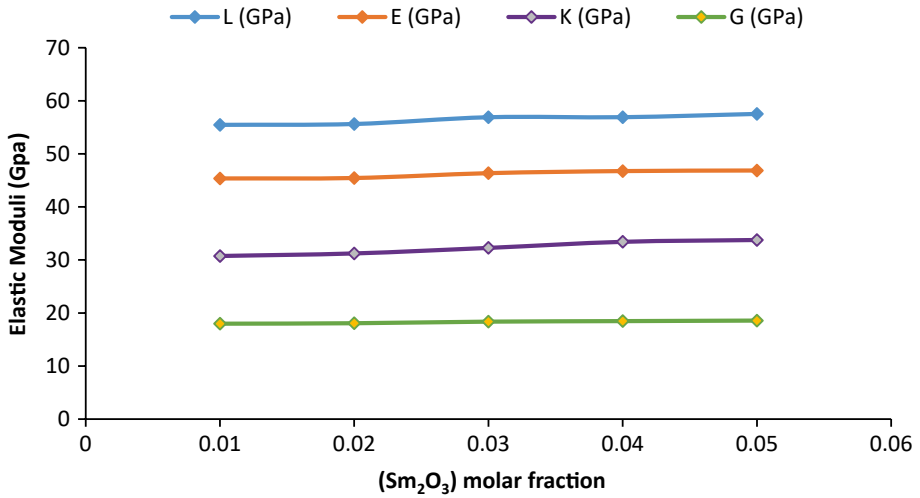


Fig. 6 Elastic moduli for [(TeO₂)_{0.7} (ZnO)_{0.3}]_{1-x} [Sm₂O₃]_x glass system

Table 3 Poisson's ratio (σ), Fugacity (f_g), Debye temperature (θ_D) and Softening temperature (T_s) for [(TeO₂)_{0.7} (ZnO)_{0.3}]_{1-x} [Sm₂O₃]_x glass system

| Molar frac. (Sm ₂ O ₃) | σ | f_g | T_s (K) | θ_D (K) |
|---|----------|-------|-----------|----------------|
| 0.01 | 0.254 | 0.095 | 749 | 289 |
| 0.02 | 0.257 | 0.093 | 725 | 300 |
| 0.03 | 0.265 | 0.086 | 754 | 303 |
| 0.04 | 0.261 | 0.090 | 754 | 301 |
| 0.05 | 0.261 | 0.090 | 756 | 301 |

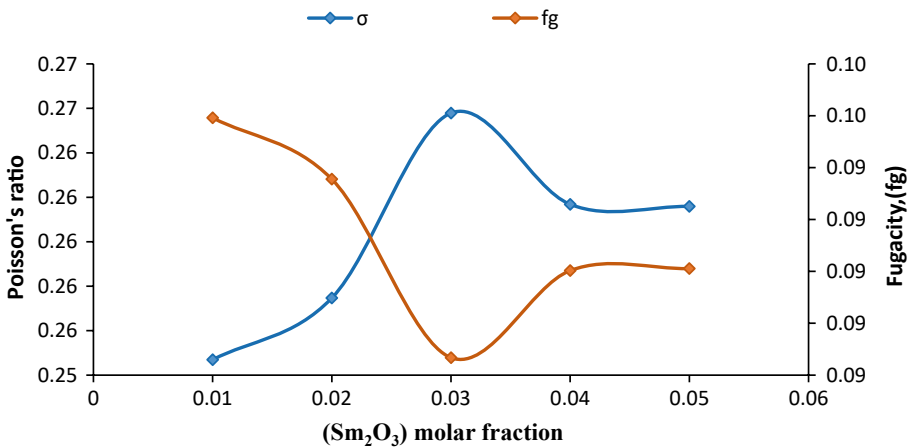


Fig. 7 Poisson's ratio and fugacity for [(TeO₂)_{0.7} (ZnO)_{0.3}]_{1-x} [Sm₂O₃]_x glass system

a more tightly packed glass system (Kannappan et al. 2009). Furthermore, the observed decrease in Poisson's ratio at certain concentrations can be attributed to the gradual increase in the average cross-link density. This increase in cross-link density contributes to the deformation and distortion of the glass network, resulting in the decrease in Poisson's ratio (Sidek et al. 2007).

Another crucial parameter investigated in this study is fugacity, which represents the fluctuation free volume in the glass system. Fugacity is influenced by the changes in Poisson's ratio and serves as a measure of the rigidity of the glass network (Saddeek et al. 2005). Figure 7 illustrates the variation of fugacity, as presented in Table 3. The fugacity values decrease in the molar fraction range of 0.01 to 0.03 and increase from 0.03 to 0.05 with the addition of more dopants. The decrease in fugacity signifies a reduction in glass rigidity and connectivity, resulting from the formation of NBOs in the glass structure (Saddeek et al. 2005). The observed increase in fugacity is attributed to the formation of more bridging oxygen (BO) in the glass system, as stated in Sidkey and Gaafar (2004). This increase enhances the glass rigidity and connectivity.

4.4 Debye temperature (θ_D) and Softening temperature (T_S)

Debye temperature is an important parameter that characterizes the lattice vibrations in a solid. It signifies the temperature at which almost all vibration modes in a solid are excited (Bahari et al. 2013). Debye temperature is a significant parameter for analyzing solid materials like glass. A decrease in its values suggests a decrease in the rigidity of the glass system. Figure 8 illustrates the behavior of Debye temperature, as recorded in Table 3, at various dopant concentrations. The values of Debye temperature generally increase with increasing dopants, with a slight decrease observed at 0.04 molar fractions. The increase in Debye temperature indicates an enhancement in the rigidity of these glasses, which can be attributed to the increase in the number of atoms in the glass system's chemical formula and the rise in the mean ultrasonic velocity (Halimah et al. 2005). The observed decrease in Debye temperature in this study can be primarily attributed to two factors: the change in the number of atoms per unit volume and the presence of non-bridging oxygen in the glass system. These factors influence the vibrational modes and overall dynamics of the

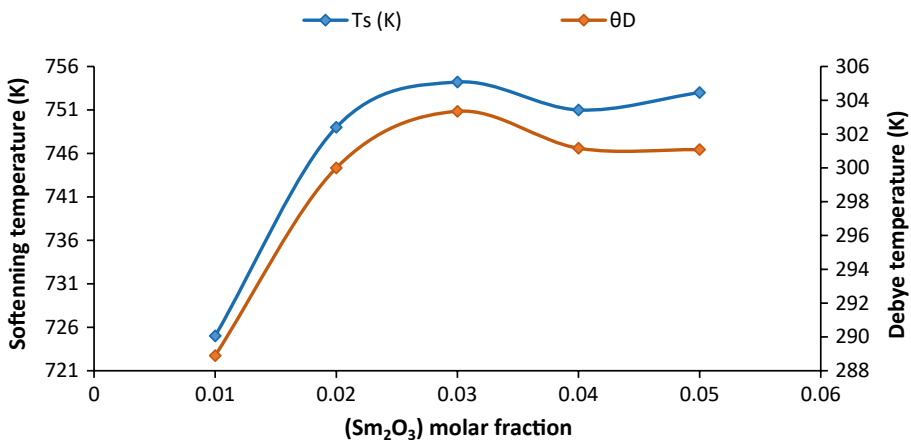


Fig. 8 Softening temperature and Debye temperature for $[(\text{TeO}_2)_{0.7} (\text{ZnO})_{0.3}]_{1-x} [\text{Sm}_2\text{O}_3]_x$ glass system

lattice, leading to a decrease in the Debye temperature (Saddeek 2004). Furthermore, the reduction of bond strength is recognized as one of the significant factors contributing to the decrease in Debye temperature, as reported by Hasnimulyati et al. (2017). When the bond strength decreases, it affects the overall vibrational behavior and leads to a lower Debye temperature in the material. Softening temperature is a critical parameter that signifies the transition from viscous flow to plastic flow in a material. It serves as an indicator of the temperature stability of the glass system, marking the temperature at which the material undergoes a change in its flow behavior (Halimah et al. 2005). Higher values of softening temperature play a significant role in determining the stability of glass materials, as indicated in El-Mallawany and Abd El-Moneim (1998). The softening temperature data for the glass system are presented in Table 3 and Fig. 8. It is observed that the values of softening temperature increase with the addition of more dopants. This increase can be attributed to the greater number of atoms in the chemical formula and higher ultrasonic velocities of the glass system, indicating a strengthening effect due to the formation of bridging oxygen (Eevon et al. 2016). However, there is a slight decrease in softening temperature at 0.04 molar fractions. This decrease indicates that the glass becomes less rigid at that concentration, which can be attributed to the creation of NBOs (Halimah et al. 2010).

5 Theoretical elastic properties

The elastic properties are also analyzed using the theoretical models. Four different theoretical elastic models were employed to assess the structure and compare the elastic moduli with the corresponding experimental values.

5.1 Makishima and mackenzie model

The Makishima-Mackenzie theoretical elastic model was used to analyze the elastic modulus of oxide glasses. This model takes into account the chemical composition of the glasses, as well as two key parameters: the packing density (V_i) and dissociation energy (G_i) of the constituent oxides per unit volume. The values of packing density and dissociation energy for all the chemical oxides are presented in Table 4.

Table 5 provides the values of total packing density, total dissociation energy, Poisson's ratio, and elastic moduli. Figure 9 displays the graph illustrating the relationship between total packing density and total dissociation energy with varying dopant concentrations.

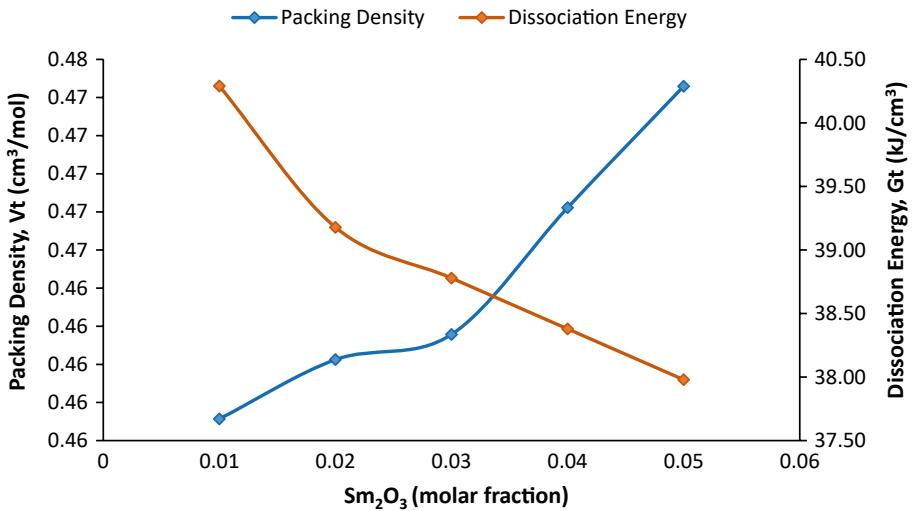
The packing density of Sm_2O_3 glasses exhibits a gradual increase as the dopant concentration increases. This rise in packing density can be attributed to the increase in glass rigidity and density of the fabricated samples. The presence of Sm^{3+} ions occupying the interstices in the glass network structure leads to a closely packed structure, thereby increasing the glass packing density (Bootjomchai 2015). Furthermore, the increase in

Table 4 Packing density (V_i) and dissociation energy (G_i) for $[(\text{TeO}_2)_{0.7}(\text{ZnO})_{0.3}]_{1-x}[\text{Sm}_2\text{O}_3]_x$ glass system

| Chemical oxides | $V_i \times 10^{-6}$ (m ³ /mol) | $G_i \times 10^9$ (J/m ³) |
|--------------------------------|--|---------------------------------------|
| TeO ₂ | 1.4288 | 35.7502 |
| ZnO | 7.9449 | 49.8435 |
| Sm ₂ O ₃ | 2.7484 | 71.2452 |

Table 5 Total packing density (V_t), total dissociation energy (G_t), young modulus (E_{mm}), bulk modulus (K_{mm}), shear modulus (G_{mm}) and Poisson's ratio (σ_{mm}) for $[(TeO_2)_{0.7}(ZnO)_{0.3}]_{1-x}[Sm_2O_3]_x$ glass system

| Molar frac. (Sm_2O_3) | V_t | $G_t \times 10^9$ (J/m ³) | E_{mm} (GPa) | K_{mm} (GPa) | G_{mm} (GPa) | σ_{mm} |
|---------------------------|-------|---------------------------------------|----------------|----------------|----------------|---------------|
| 0.01 | 0.457 | 40.290 | 36.837 | 20.207 | 15.397 | 0.196 |
| 0.02 | 0.460 | 39.178 | 36.063 | 19.918 | 15.048 | 0.198 |
| 0.03 | 0.461 | 38.778 | 35.798 | 19.828 | 14.927 | 0.199 |
| 0.04 | 0.468 | 38.379 | 35.939 | 20.193 | 14.932 | 0.203 |
| 0.05 | 0.474 | 37.979 | 36.049 | 20.530 | 14.929 | 0.207 |

**Fig. 9** Packing density and dissociation energy for $[(TeO_2)_{0.7}(ZnO)_{0.3}]_{1-x}[Sm_2O_3]_x$ glass system

packing density can be attributed to the variations in glass network structure around the dopant cations, which result in an increase in their cation field strength. This change in the network configuration contributes to the higher packing density observed in the samples (Abd Elfadeel et al. 2017).

The strong polarization of the cations in the glass network leads to increased ion–dipole interactions, thereby enhancing the packing density. On the other hand, the dissociation energy per unit volume (G_t) decreases with an increase in dopant concentration, as indicated in Table 5. This decrease in dissociation energy is associated with a reduction in the rigidity of the glass structure. The Makishima and Mackenzie model also calculates the elastic moduli and Poisson's ratio based on the packing density and dissociation energy per unit volume. The values of these parameters are provided in Table 5, and their corresponding graphs are depicted in Figs. 10 and 11, showcasing the variations at different dopant concentrations.

The elastic moduli, including Young's modulus, bulk modulus, and shear modulus, generally decrease with increasing dopant concentration, with a slight increase observed at 0.04 molar fractions. This decreasing trend in elastic moduli is attributed to the

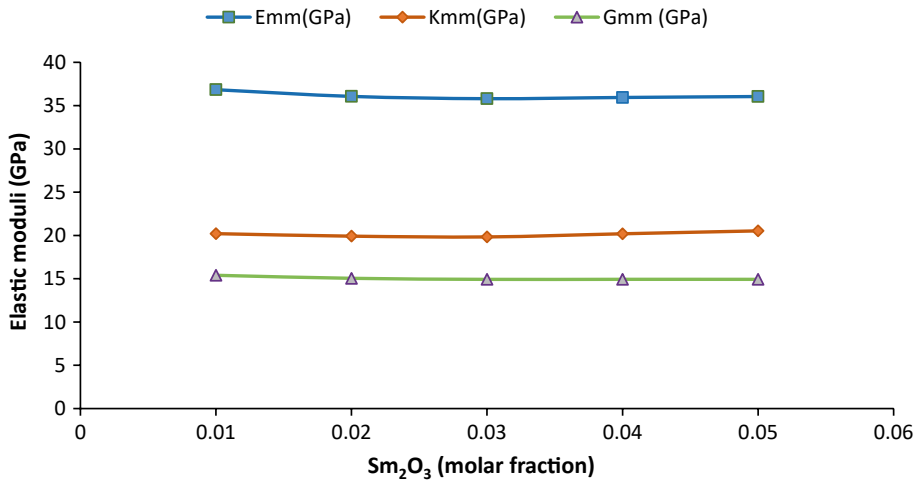


Fig. 10 Makishima and Mackenzie elastic moduli for $[(\text{TeO}_2)_{0.7}(\text{ZnO})_{0.3}]_{1-x}[\text{Sm}_2\text{O}_3]_x$ glass system

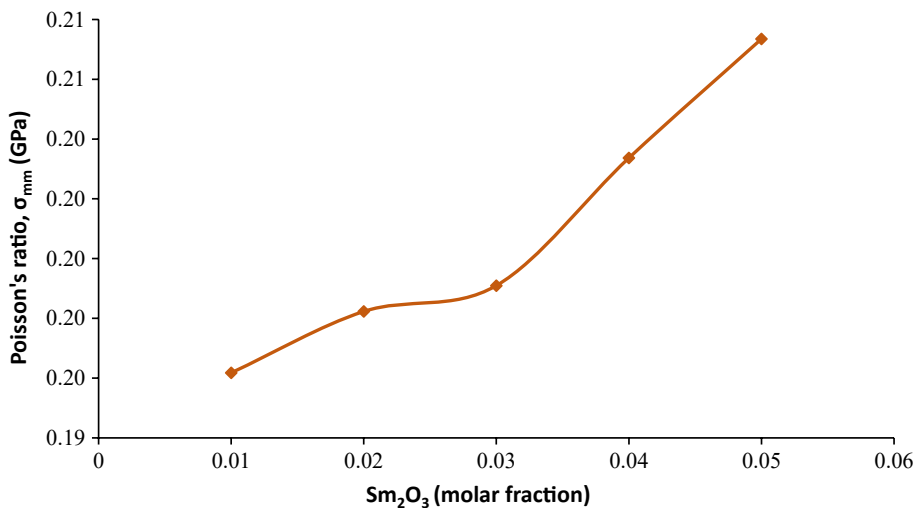
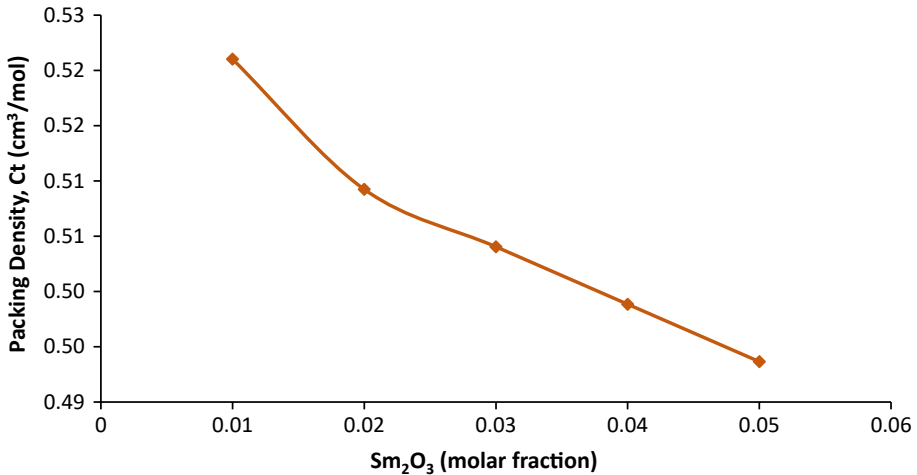


Fig. 11 Makishima and Mackenzie Poisson's ratio for $[(\text{TeO}_2)_{0.7}(\text{ZnO})_{0.3}]_{1-x}[\text{Sm}_2\text{O}_3]_x$ glass system

decrease in glass rigidity and the dissociation energy per unit volume of the glass system. However, the observed increase in elastic moduli can be attributed to the increase in glass packing density (Hasnimulyati et al. 2017). Moreover, the glass network's elevated field strength can additionally induce an increase in the stiffness of the glass structure, consequently leading to enhanced bond strength and increased elastic moduli (El-Mallawany and Abd El-Moneim 1998). According to Table 5, there is a noticeable upward trend in the Poisson's ratio as the concentration of dopants increases. The observed increase in the Poisson's ratio aligns with the corresponding packing density

Table 6 Packing density (C_t), Young modulus (E_{rm}), bulk modulus (K_{rm}), shear modulus (G_{rm}) and Poisson's ratio (σ_{rm}) for $[(TeO_2)_{0.7}(ZnO)_{0.3}]_{1-x}[Sm_2O_3]_x$ glass system

| Molar frac. (Sm_2O_3) | C_t | E_{rm} (GPa) | K_{rm} (GPa) | G_{rm} (GPa) | σ_{rm} |
|---------------------------|-------|----------------|----------------|----------------|---------------|
| 0.01 | 0.521 | 41.984 | 26.249 | 17.019 | 0.233 |
| 0.02 | 0.509 | 39.902 | 24.384 | 16.256 | 0.227 |
| 0.03 | 0.504 | 39.092 | 23.645 | 15.963 | 0.224 |
| 0.04 | 0.498 | 38.290 | 22.921 | 15.672 | 0.221 |
| 0.05 | 0.493 | 37.497 | 22.212 | 15.384 | 0.218 |

**Fig. 12** Rocherulle packing density for $[(TeO_2)_{0.7}(ZnO)_{0.3}]_{1-x}[Sm_2O_3]_x$ glass system

of the glass system, indicating a similar behavior. This rise can also be attributed to the tightly packed structure of the synthesized glasses (Makishima and Mackenzie 1975).

5.2 Rocherulle model

The Rocherulle model made certain modifications to the packing density calculation initially proposed by Makishima and Mackenzie. In this model, we opted to consider the density of each individual oxide constituent rather than the density of the synthesized glass. Table 6 presents the packing density, Young's modulus, and Poisson's ratio calculated using this model. Figure 12 illustrates the relationship between packing density and dopant concentration as predicted by this model.

With the increase in the dopant amount, the modified packing density demonstrates a continuous decrease. This decline in packing density can be attributed to the lower density value ($C_t=2.7484$) of Sm_2O_3 in comparison to that of the glass system, resulting in a reduction in Young's modulus (Saddeek 2004). The packing density obtained from the Rocherulle model is comparatively higher than the overall packing density derived from the Makishima and Mackenzie models. Figure 13 presents a plot depicting the elastic moduli for this model at various dopant concentrations.

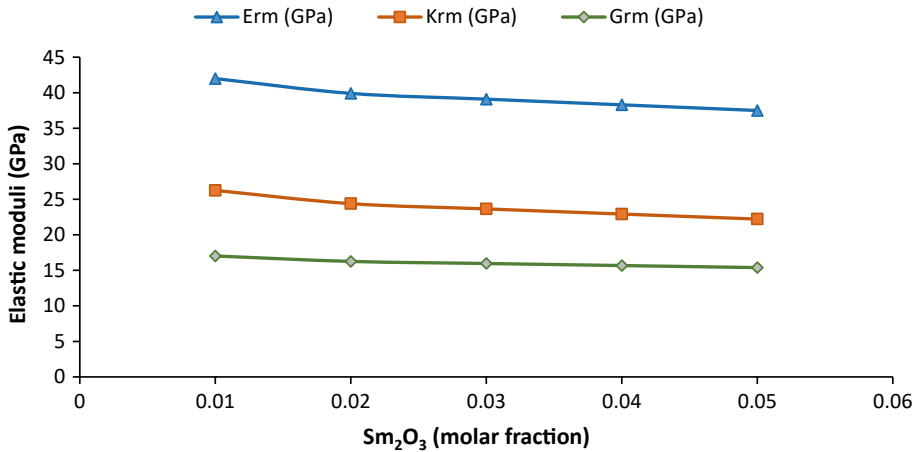


Fig. 13 Rocherulle elastic moduli for $[(\text{TeO}_2)_{0.7}(\text{ZnO})_{0.3}]_{1-x}[\text{Sm}_2\text{O}_3]_x$ glass system

The Young's modulus and Poisson's ratio values, as presented in Table 6, exhibit a decreasing trend as the dopant concentration increases. This decrease can be attributed to the corresponding decrease in the packing density of the fabricated glasses, resulting in a decrease in the overall stiffness of the glass (Hasnimulyati et al. 2017). Figure 14 illustrates the graph depicting the relationship between the Poisson's ratio and various dopant concentrations.

5.3 Bond compression model

In Bond compression model, the data for various oxides, including coordination number, bond length, number of cations per glass formulation, and oxide unit for each component,

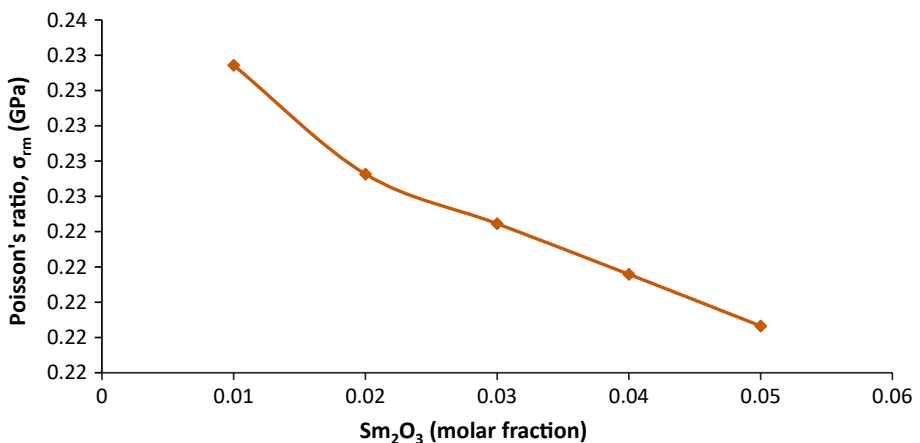


Fig. 14 Rocherulle Poisson's ratio for $[(\text{TeO}_2)_{0.7}(\text{ZnO})_{0.3}]_{1-x}[\text{Sm}_2\text{O}_3]_x$ glass system

were collected and reported. The elastic modulus of the composite glass is then calculated utilizing the data provided in Table 7.

The elastic moduli obtained through the Bond compression model incorporate several factors, including the total number of cations per glass formula unit (η), the number of network bonds per unit volume (n_b), and the average cross-link density per unit formula (\bar{n}_c) of the synthesized glasses, as presented in Table 8.

Table 8 reveals that the average density of cross-links per unit formula exhibits a consistent increase with an escalating dopant concentration. This behavior can be attributed to the incorporation of Sm_2O_3 , which possesses a high coordination number, thereby enhancing the dimensionality of the network structure and resulting in a higher average density of cross-links per unit formula. Additionally, as indicated in Table 8, the reported number of bonds per unit volume (n_b) also increases with dopant concentration. This rising trend can be attributed to the creation of BO, which contributes to greater compactness and rigidity within the synthesized glass network. The computed elastic moduli of the Bond compression model are presented in Table 9. Furthermore, Fig. 15 depicts the corresponding graphs.

With the addition of more dopants, the elastic moduli exhibited a decrease within the 0.01 to 0.03 molar fraction range, followed by an increase at 0.04 and 0.05 molar fractions. It is worth noting that the elastic moduli obtained through the bond compression model are generally larger in comparison to their corresponding experimental values. This behavior is expected and has been reported in numerous literature sources,

Table 7 First order stretching force constant (f), number of cross link density per cation (n_c), number of cations per glass formula unit (N_c), coordination number (n_f) and bond length (r)

| Oxides | $f(N_m - 1)$ | n_c | N_c | n_f | r (nm) | Reference |
|-------------------------|--------------|-------|-------|-------|----------|----------------------|
| TeO_2 | 215.719 | 2 | 1 | 4 | 0.199 | Saddeek et al. 2005) |
| ZnO | 219.004 | 4 | 1 | 6 | 0.198 | Awasthi et al. 2005) |
| Sm_2O_3 | 110.116 | 4 | 2 | 6 | 0.249 | Mawlud et al. 2017) |

Table 8 Total number of cations per glass formula unit (η), number of network bond per unit volume (n_b) (m^{-3}) and average cross link density per unit formula (\bar{n}_c) for $[(\text{TeO}_2)_{0.7}(\text{ZnO})_{0.3}]_{1-x}[\text{Sm}_2\text{O}_3]_x$ glass system

| Molar frac (Sm_2O_3) | η | \bar{n}_c | $n_b \times 10^{28}$ |
|--|--------|-------------|----------------------|
| 0.01 | 1.010 | 2.627 | 10.011 |
| 0.02 | 1.020 | 2.654 | 10.139 |
| 0.03 | 1.030 | 2.681 | 10.168 |
| 0.04 | 1.040 | 2.707 | 10.197 |
| 0.05 | 1.050 | 2.733 | 10.226 |

Table 9 Elastic moduli, Poisson's ratio and ratio K_{bc}/K_e for $[(\text{TeO}_2)_{0.7}(\text{ZnO})_{0.3}]_{1-x}[\text{Sm}_2\text{O}_3]_x$ glass system

| Molar frac. (Sm_2O_3) | L_{bc} (GPa) | E_{bc} (GPa) | K_{bc} (GPa) | G_{bc} (GPa) | σ_{bc} | K_{bc}/K_e |
|---|----------------|----------------|----------------|----------------|---------------|--------------|
| 0.01 | 184.372 | 161.510 | 96.109 | 66.197 | 0.219 | 3.126 |
| 0.02 | 183.709 | 161.062 | 95.650 | 66.044 | 0.219 | 3.062 |
| 0.03 | 182.353 | 160.001 | 94.835 | 65.638 | 0.218 | 2.850 |
| 0.04 | 183.106 | 160.786 | 95.121 | 65.989 | 0.218 | 2.934 |
| 0.05 | 183.737 | 161.460 | 95.345 | 66.293 | 0.217 | 2.910 |

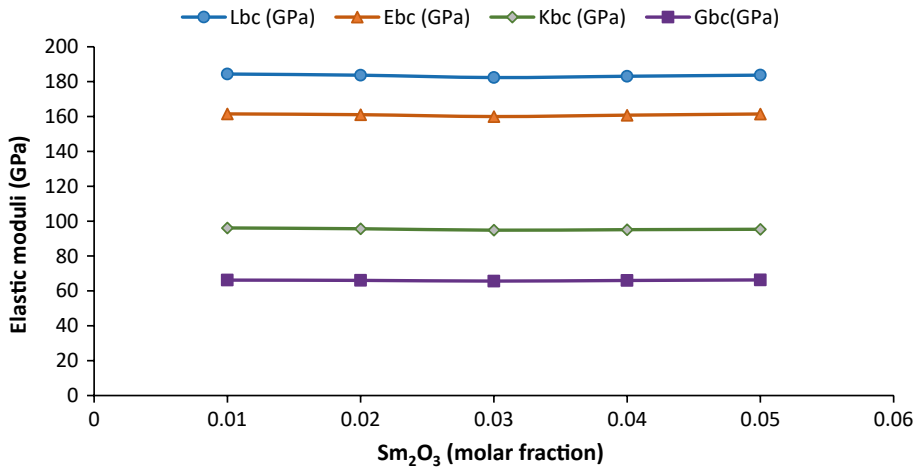


Fig. 15 Bond compression elastic moduli for $[(\text{TeO}_2)_{0.7}(\text{ZnO})_{0.3}]_{1-x}[\text{Sm}_2\text{O}_3]_x$ glass system

stating that the moduli obtained using this model can be higher by a factor of 3 to 10 compared to the experimental moduli (El-Mallawany and Abd El-Moneim 1998). In cases where the elastic moduli values increase, there is a concurrent decrease in molar volume, leading to the production of closely packed and rigid structures in the synthesized glasses. Consequently, there is an increase in the number of network bonds per unit volume. Conversely, the decrease in elastic moduli at certain concentrations can be attributed to an increase in molar volume resulting from an increasing dopant concentration. Among all the estimated moduli, the bulk modulus (K_{bc}) is found to be the most significant for the geometrical study of the glass structure, earning the model the occasional designation of the bulk compression model. As indicated by Sidkey and Gaafar (2004), the observed increase can be explained by the K_{bc} parameter, which depends on the number of network bonds per unit volume and the first-order stretching force constant. In Table 9, the values of K_{bc}/K_e exhibit a decrease from 3.126 at 0.01 to 2.910 at 0.05 molar fractions, except for the 0.04 molar fraction where the value increases. The obtained values fall within the ranges reported for tellurium oxide-based glasses, as revealed by El-Mallawany (1998). According to the literature, the ratio of K_{bc}/K_e falls within the range of 1–3 for an ideal isotropic compression mechanism and 3–10 for ring deformation mechanisms. Based on this information, it can be inferred that the current glass systems undergo isotropic ring compression, as illustrated in Fig. 16.

The Poisson's ratio exhibits a gradual decrease from 0.219 at 0.01 to 0.217 at 0.05 molar fractions, corresponding to the increase in dopants, as indicated in Table 9 and depicted in Fig. 17. The relationship utilized in calculating the Poisson's ratio within the bond compression model highlights its dependency on the average cross-link density, which justifies the observed behavior. Consequently, the decrease in Poisson's ratio can be attributed to the increase in the average cross-link density within the glass system. This outcome aligns with expectations, as an increase in average cross-link density implies the presence of more bonds in the lateral direction, enhancing resistance to lateral strain and thereby reducing the Poisson's ratio of the glass (Sidkey and Gaafar 2004).

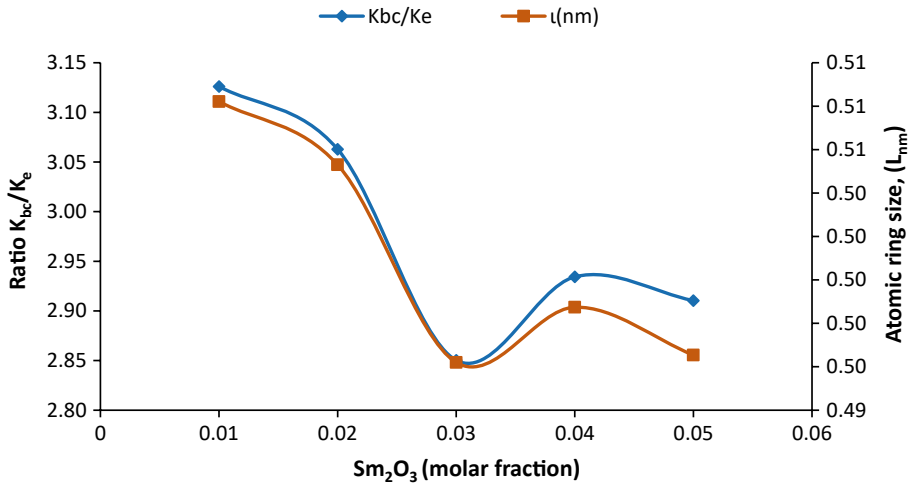


Fig. 16 Ratio of K_{bc}/K_e and atomic ring size l for $\{[(TeO_2)_{0.7}(ZnO)_{0.3}]_{1-x}\} [Sm_2O_3]_x$ glass system

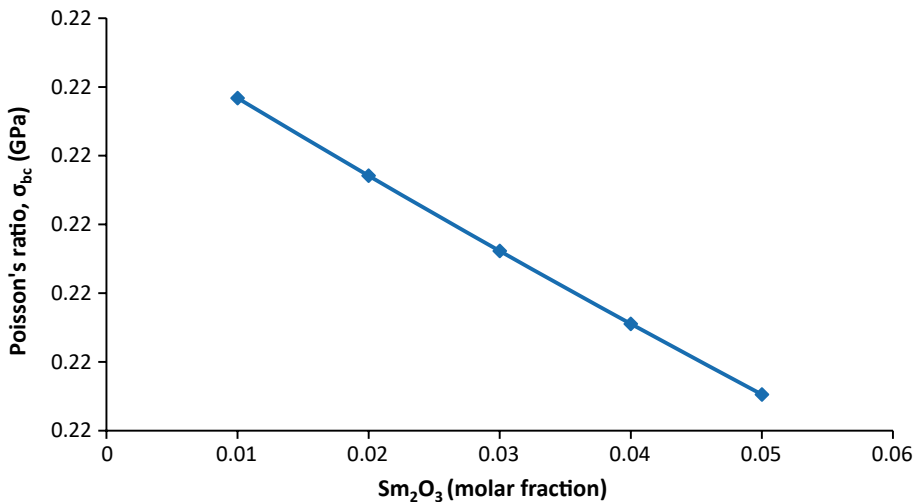


Fig. 17 Bond compression Poisson's ratio for $\{[(TeO_2)_{0.7}(ZnO)_{0.3}]_{1-x}\} [Sm_2O_3]_x$ glass system

5.4 Ring deformation model

The ring deformation model is an adapted version of the bulk compression model, relying on the K_{bc}/K_e value ratio. It has been observed that higher values of K_{bc}/K_e lead to the formation of a layer or chain network, suggesting that the network bond bending process becomes prominent under bulk compression conditions (Azlan et al. 2017b). In this model, the atomic ring size (l) is directly proportional to K_{bc}/K_e , which is calculated using the average stretching force constant and the measured bulk modulus. An increase in the atomic ring size signifies the potential for bond bending within the glass system. Table 10

Table 10 Average stretching force constant, atomic ring size for $[(\text{TeO}_2)_{0.7}(\text{ZnO})_{0.3}]_{1-x}[\text{Sm}_2\text{O}_3]_x$ glass system

| Molar frac. (Sm_2O_3) | $\bar{F}(\text{Nm}^{-1})$ | $l(\text{nm})$ |
|---|---------------------------|----------------|
| 0.01 | 215.615 | 0.508 |
| 0.02 | 214.233 | 0.505 |
| 0.03 | 212.860 | 0.496 |
| 0.04 | 211.495 | 0.498 |
| 0.05 | 210.138 | 0.496 |

presents the values of atomic ring size and average stretching force constant for the synthesized glasses.

Figure 16 illustrates the correlation between atomic ring size and dopant concentration. As the concentration of dopants increases, the values of atomic ring size decrease. This trend in atomic ring size aligns with the trend observed in K_{bc}/K_c ratio values, providing further evidence of the direct relationship between these two parameters. A larger atomic ring size indicates a more compact glass structure. Table 11 presents the elastic moduli and Poisson’s ratio for this model, while Figs. 18 and 19 display their respective graphs against dopant concentration. With an increase in dopants, the elastic moduli show an upward trend. In this model, the increasing trend of the elastic moduli can be attributed to the behavior of their molar volume. Higher molar volume values lead to the formation of

Table 11 Ring deformation elastic moduli, Poisson’s ratio for $[(\text{TeO}_2)_{0.7}(\text{ZnO})_{0.3}]_{1-x}[\text{Sm}_2\text{O}_3]_x$ glass system

| Molar frac. (Sm_2O_3) | $L_{rd}(\text{GPa})$ | $E_{rd}(\text{GPa})$ | $K_{rd}(\text{GPa})$ | $G_{rd}(\text{GPa})$ | σ_{rd} |
|---|----------------------|----------------------|----------------------|----------------------|---------------|
| 0.01 | 47.751 | 43.582 | 25.934 | 17.862 | 0.219 |
| 0.02 | 50.441 | 44.223 | 26.262 | 18.134 | 0.219 |
| 0.03 | 53.287 | 46.755 | 27.712 | 19.181 | 0.218 |
| 0.04 | 52.116 | 45.763 | 27.073 | 18.781 | 0.218 |
| 0.05 | 52.602 | 46.224 | 27.296 | 18.979 | 0.217 |

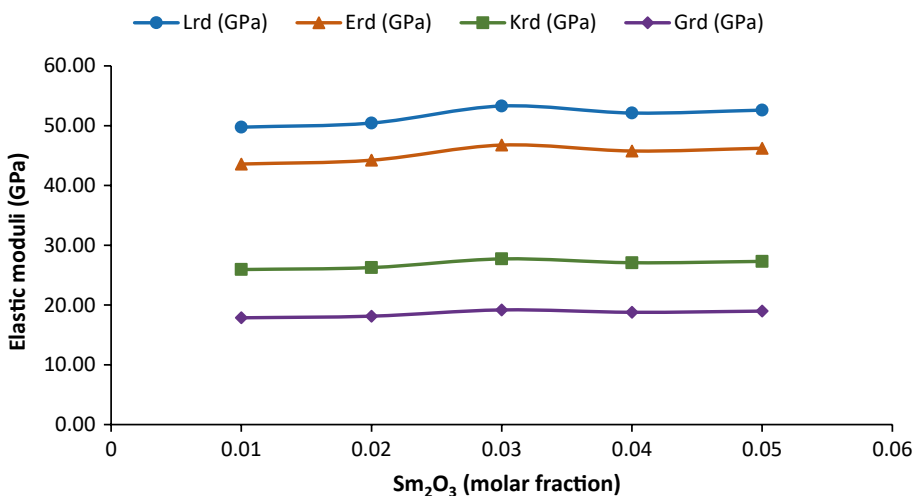


Fig. 18 Ring deformation elastic moduli for $[(\text{TeO}_2)_{0.7}(\text{ZnO})_{0.3}]_{1-x}[\text{Sm}_2\text{O}_3]_x$ glass system

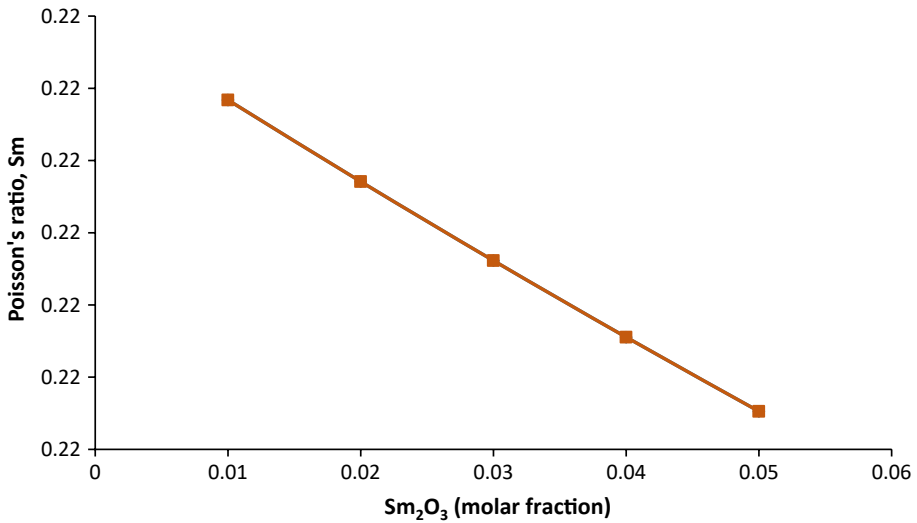


Fig. 19 Ring deformation Poisson's ratio for $[(\text{TeO}_2)_{0.7} (\text{ZnO})_{0.3}]_{1-x} [\text{Sm}_2\text{O}_3]_x$ glass system

closely packed and rigid structures within the glass system (Gaafar et al. 2011). As dopants increase, the Poisson's ratio decreases, indicating a relationship with the cross-link density of the glass system.

The theoretical and experimental data of elastic moduli were compared, and their analysis is presented and depicted in Figs. 20, 21, 22. Upon comparing the theoretical and experimental elastic moduli, it is evident that all calculated elastic moduli from the theoretical models align closely with the experimental elastic moduli, with the exception of the Bond compression elastic moduli. However, it is worth noting that the Bond compression elastic moduli are still considered valid, as long as their values are higher than the experimental values by a factor of 3–10, as mentioned by El-Mallawany (1998). This comparison highlights the level of agreement between the experimental and calculated elastic moduli. It can be concluded that the experimental results demonstrate a very good agreement with the theoretical models.

6 Judd-Ofelt intensity parameters

The incorporation of RE-ions into the host materials can be quantitatively assessed through the application of Judd-Ofelt theory. By utilizing experimental data to establish the initial absorption state, which determines the electrical dipole intensity under specific conditions, it becomes possible to measure three parameters (Ω_2 , Ω_4 and Ω_6) (Li et al. 2019). In this investigation, the J-O parameters are employed to gather data regarding chemical and physical characteristics of Sm^{3+} ions embedded into the glass network. The Ω_2 parameter provides insights into the covalency of Sm^{3+} bond within the glass matrix and the asymmetries surrounding Sm^{3+} ions. Consequently, there exists an inverse relationship between the Ω_6 parameter and covalency of Sm^{3+} bond. The J-O parameters Ω_4 and Ω_6 have a significant impact on glass properties such as dielectric constant and glass viscosity, as they are influenced by the vibronic transition of Sm^{3+} ions coupled to the ligand atoms.

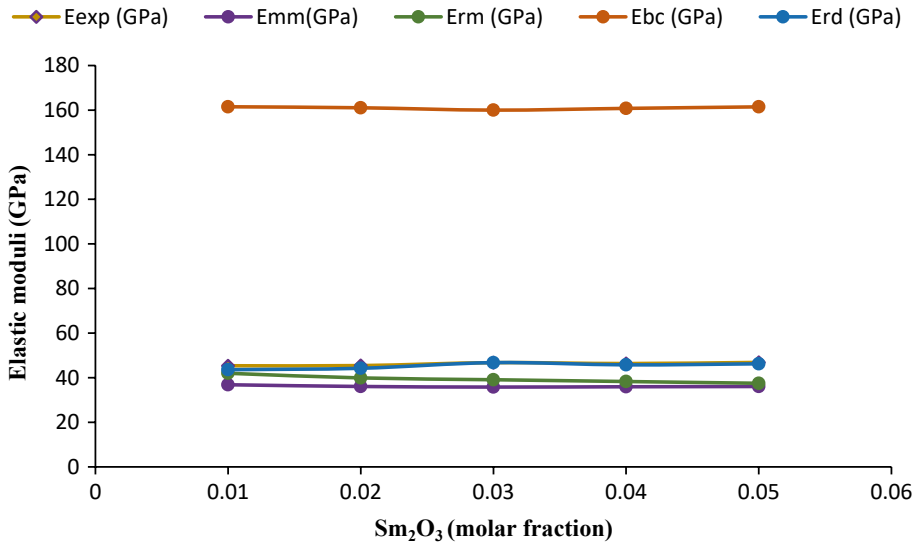


Fig. 20 Correlation of the experimental young modulus with theoretical young moduli for $[(TeO_2)_{0.7}(ZnO)_{0.3}]_{1-x}[Sm_2O_3]_x$ glass system

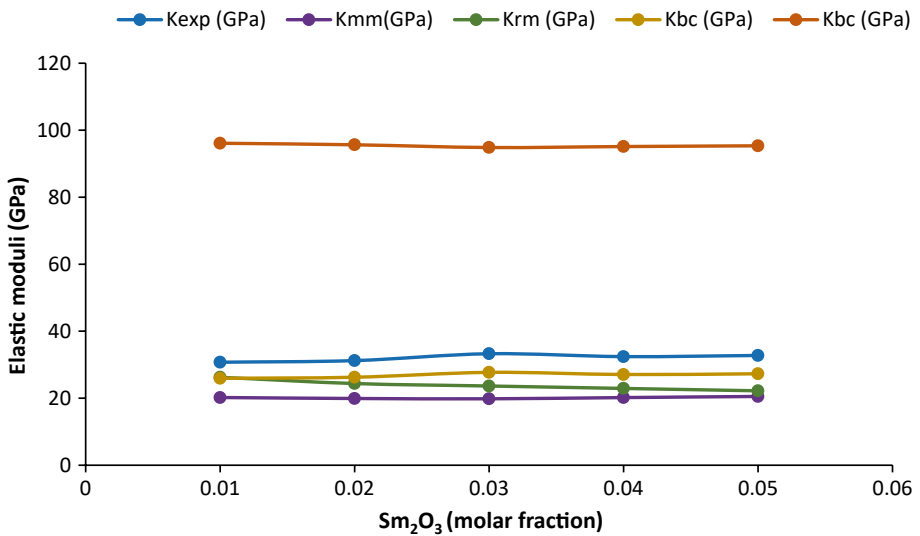


Fig. 21 Correlation of the experimental Bulk modulus with theoretical Bulk moduli for $[(TeO_2)_{0.7}(ZnO)_{0.3}]_{1-x}[Sm_2O_3]_x$ glass system

Moreover, the stiffness of the host material housing the Sm^{3+} ions is interconnected with Ω_4 and Ω_6 (Mawlud et al. 2017).

The J-O (Ω_2 , Ω_4 and Ω_6) parameters are then used to calculate other radiative parameters such as branching ratio (β_R), magnetic dipole radiative transition probability (A_{MD}), electric dipole radiative transition probability (A_{ED}), gain bandwidth ($\Delta\lambda_{eff} \times \sigma_p$) and

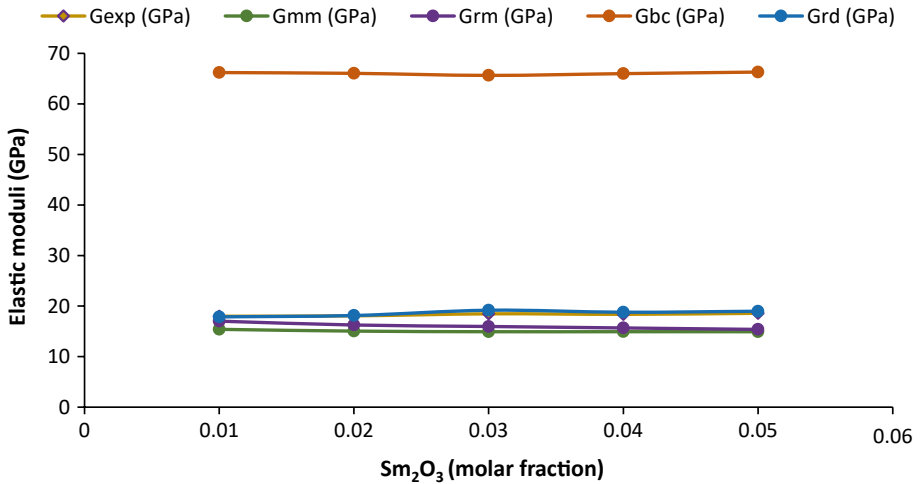


Fig. 22 Correlation of the experimental Shear modulus with theoretical Shear moduli for [(TeO₂)_{0.7}(ZnO)_{0.3}]_{1-x}[Sm₂O₃]_x glass system

optical gain ($\sigma_p \times \tau$). As stated in Mawlud et al. (2017), these properties are utilized to ascertain the likely laser transitions of rare-earth ions within the host material. Table 12 shows the computed values of J-O parameters (Ω_2 , Ω_4 and Ω_6) as well as the spectroscopic quality factor Ω_4/Ω_6 of the synthesized glass samples.

The J-O parameters are found to be exhibiting an order i.e. $\Omega_2 > \Omega_4 > \Omega_6$ with an increase in the dopant concentration, Ω_2 demonstrates an upward trend. This rise in Ω_2 values can be attributed to the presence of strong covalent bonding within the glass system. The higher Ω_2 values also suggest a decrease in ionicity and an increase in the asymmetry of rare-earth (RE) ions in relation to their surrounding ligands (Li et al. 2019). With an increase in dopant concentration, both Ω_4 and Ω_6 display an ascending trend, although there are certain concentrations where the values decrease. The upward trend in Ω_4 and Ω_6 suggests enhanced rigidity and viscosity within the glass matrix.

According to Tanko et al. 2016a, the decreasing values of Ω_4 and Ω_6 indicate that vibronic transitions between the ligand atoms and rare-earth ions have an impact on viscosity. Materials with a better spectroscopic quality factor (Ω_4/Ω_6) are advantageous for investigating the active laser medium (Li et al. 2019). In Table 12, the values of (Ω_4/Ω_6) are presented, and each value is observed to be greater than 1, with the highest value recorded

Table 12 The JuddOfelt intensity parameters and spectroscopic quality factor for [(TeO₂)_{0.7}(ZnO)0.3]_{1-x}[Sm₂O₃]_x glass system

| Molar frac. Sm ₂ O ₃ | $\Omega_2 (\times 10^{-20} \text{ cm}^2)$ | $\Omega_4 (\times 10^{-20} \text{ cm}^2)$ | $\Omega_6 (\times 10^{-20} \text{ cm}^2)$ | Ω_4/Ω_6 |
|--|---|---|---|---------------------|
| 0.01 | 57.367 | 4.970 | 3.255 | 1.527 |
| 0.02 | 58.071 | 5.256 | 3.477 | 1.511 |
| 0.03 | 58.771 | 5.856 | 3.777 | 1.550 |
| 0.04 | 59.471 | 5.023 | 4.234 | 1.186 |
| 0.05 | 60.978 | 5.577 | 4.706 | 1.185 |

as 1.550. The obtained higher value of (Ω_4/Ω_6) indicates that the examined glass samples serve as superior optical media for active laser applications (Tanko et al. 2016b). Table 13 provides a comparison between the experimental and measured line strengths, demonstrating the validity of the fitting process. Additionally, the small root-mean-square deviation values (δ_{rms}) of the experimental and calculated oscillator strengths indicate a strong correspondence between the two values, confirming the accuracy of the Judd-Ofelt intensity parameters and the overall validity of the analysis.

To assess the validity of the fitting, the experimental and computed line strengths were compared with existing literature (Azlan et al. 2017a). The calculations were performed following the methodology employed in the majority of previously reported studies on Sm_2O_3 doped glasses found in the literature (Ahmadi et al. 2017). The minimal difference observed between the calculated and experimental spectral intensities, as indicated by the (δ_{rms}) values, highlights the exceptional agreement between the calculated and experimental line strengths (Ahmadi et al. 2017). The small values of (δ_{rms}) further indicate a robust fit between the experimental and estimated spectral intensities, affirming the validity of the Judd-Ofelt intensity parameters (Mawlut et al. 2017).

As per the reference (Seshadri et al. 2015), the spectral intensities exhibit variations at different concentrations, indicating varying degrees of crystal field asymmetry. To explore the potential applications of the prepared glasses, additional calculations were performed to determine the magnetic dipole radiative transition probability (A_{MD}), electric dipole radiative transition probability (A_{ED}), branching ratio (β_R), gain bandwidth ($\Delta\lambda_{eff} \times \sigma_p$), and optical gain ($\sigma_p \times \tau$). These calculations were based on the methodologies commonly employed in relevant literature. The outcomes of these calculations are presented in Table 14.

In the present glass system, the transition ${}^6\text{H}_{7/2}$ has recorded the highest radiative transition rate when compared with other transitions and thus, making it ideal for laser emission (Li et al. 2019). Transitions with the highest values of radiative transition probabilities are associated with large branching ratios. The luminescence branching ratio serves as a characterization of the lasing power of a transition (Mawlut et al. 2017). The ${}^4\text{G}_{5/2} \rightarrow {}^6\text{H}_{7/2}$ transitions demonstrate higher values of branching ratio (β_R) compared to other transitions investigated in this study, and these values are consistent with those reported in literature (Hua et al. 2022). The symmetry of the surroundings for trivalent rare-earth (RE) ions is determined by the ratio of electric dipole to magnetic dipole transition intensities (Sun et al. 2023). The evaluated asymmetry ratios for the transitions ${}^4\text{G}_{5/2} \rightarrow {}^6\text{H}_{9/2}$ and ${}^4\text{G}_{5/2} \rightarrow {}^6\text{H}_{5/2}$ decrease from 4.820 to 0.651 with increasing Sm^{3+} concentration. From the results, the dominance of the electric dipole (ED) transition over the magnetic dipole (MD) transition suggests that low asymmetry present in the sites occupied by Sm^{3+} ions within the glass. However, the 0.05 dopant level show significant asymmetry in nature. Furthermore, the relaxation from a higher state to all of its lower levels is influenced by the values of electric dipole transition probability A_{ED} and magnetic dipole transition probability A_{MD} . Consequently, transitions that possess generally higher values of A_{ED} , A_{MD} , β_R and an energy gap greater than a few photons may exhibit laser activity among all possible relaxations to lower levels (Mawlut et al. 2017).

The radiative transition probabilities indicate that ${}^4\text{G}_{5/2} \rightarrow {}^6\text{H}_{7/2}$ transition possesses the highest values, with A_{ED} measured at 863.712 S^{-1} and A_{MD} at 864.945 S^{-1} . These moderately higher values highlight the suitability of the ${}^4\text{G}_{5/2} \rightarrow {}^6\text{H}_{7/2}$ transition for laser emission compared to other transitions (Hamza et al. 2019b). Transitions with the highest radiative transition probabilities are associated with high branching ratios. As shown in Table 13, the ${}^6\text{H}_{7/2}$ transition exhibits higher β_R values. The luminescence

Table 13 Comparison between the experimental and measured line strength, root mean square deviation (δ_{rms}) for $[(\text{TeO}_2)_{0.7}(\text{ZnO})_{0.3}]_{1-x}[\text{Sm}_2\text{O}_3]_x$ glass system

| Transition | λ (1/cm) | Sm 0.01 | | Sm 0.02 | | Sm 0.03 | | Sm 0.04 | | Sm 0.05 | |
|-------------------------------------|------------------|------------------|------------------|------------------|------------------|------------------|------------------|------------------|------------------|------------------|------------------|
| | | f_{exp} | f_{cal} | f_{exp} | f_{cal} | f_{exp} | f_{cal} | f_{exp} | f_{cal} | f_{exp} | f_{cal} |
| ${}^6\text{F}_{3/2}$ | 6689 | 30.453 | 30.231 | 30.066 | 30.190 | 35.271 | 35.670 | 30.560 | 30.251 | 35.164 | 36.498 |
| ${}^6\text{F}_{5/2}$ | 7205 | 12.095 | 12.034 | 11.999 | 12.214 | 14.672 | 14.937 | 12.511 | 11.943 | 14.589 | 14.810 |
| ${}^6\text{F}_{7/2}$ | 8078 | 9.084 | 9.085 | 9.471 | 9.470 | 11.962 | 11.990 | 10.466 | 10.465 | 13.543 | 13.543 |
| ${}^6\text{F}_{9/2}$ | 9183 | 5.620 | 5.613 | 5.893 | 5.901 | 7.376 | 7.426 | 6.933 | 6.949 | 9.015 | 9.017 |
| ${}^6\text{F}_{11/2}$ | 10,438 | 0.851 | 0.896 | 0.996 | 0.943 | 1.166 | 1.185 | 1.235 | 1.129 | 1.477 | 1.465 |
| ${}^4\text{F}_{9/2}$ | 20,661 | 1.395 | 1.394 | 1.377 | 1.385 | 1.619 | 1.638 | 1.391 | 1.413 | 1.692 | 1.696 |
| ${}^4\text{F}_{7/2}$ | 24,752 | 0.237 | 0.229 | 0.329 | 0.233 | 0.328 | 0.282 | 0.493 | 0.232 | 0.344 | 0.286 |
| Δ_{rms} (10^{-6}) | | 0.008 | 0.010 | 0.070 | 0.180 | 0.280 | | | | | |

Table 14 Calculated transition probabilities [A_{MD} , A_{ED}], branching ratio (β_R), gain band width ($\Delta\lambda_{eff} \times \sigma_p$), and optical gain ($\sigma_p \times \tau$) in ${}^4G_{5/2}$ transition level of Sm^{3+} ions for $[(TeO_2)_{0.7}(ZnO)_{0.3}]_{1-x}[Sm_2O_3]_x$ glass system

| Transitions | Wavelength (cm ⁻¹) | A_{MD} (s ⁻¹) | A_{ED} (s ⁻¹) | β_R (%) | $\Delta\lambda_{eff} \times \sigma_p$ (× 10 ⁻²¹) | $\sigma_p \times \tau$ (× 10 ⁻²⁵) |
|---|--------------------------------|-----------------------------|-----------------------------|---------------|--|---|
| Sm₂O₃ (0.01) | | | | | | |
| ${}^4G_{5/2} \rightarrow$ | | | | | | |
| ${}^6H_{11/2}$ | 710 | 390.965 | 562.757 | 0.241 | 1.704 | 3.177 |
| ${}^6H_{9/2}$ | 647 | 547.322 | 758.389 | 0.326 | 1.132 | 3.174 |
| ${}^6H_{7/2}$ | 604 | 758.413 | 863.712 | 0.368 | 1.893 | 3.257 |
| ${}^6H_{5/2}$ | 566 | 157.341 | 765.432 | 0.063 | 1.657 | 3.154 |
| Sm₂O₃ (0.02) | | | | | | |
| ${}^4G_{5/2} \rightarrow$ | | | | | | |
| ${}^6H_{11/2}$ | 710 | 382.162 | 552.773 | 0.241 | 1.724 | 3.147 |
| ${}^6H_{9/2}$ | 647 | 534.541 | 743.426 | 0.326 | 1.232 | 3.124 |
| ${}^6H_{7/2}$ | 604 | 854.373 | 849.744 | 0.369 | 1.895 | 3.257 |
| ${}^6H_{5/2}$ | 566 | 153.505 | 581.231 | 0.062 | 1.647 | 3.134 |
| Sm₂O₃ (0.03) | | | | | | |
| ${}^4G_{5/2} \rightarrow$ | | | | | | |
| ${}^6H_{11/2}$ | 710 | 476.320 | 753.543 | 0.242 | 1.799 | 4.159 |
| ${}^6H_{9/2}$ | 647 | 665.209 | 601.420 | 0.327 | 1.397 | 3.823 |
| ${}^6H_{7/2}$ | 604 | 864.945 | 776.619 | 0.372 | 2.228 | 4.214 |
| ${}^6H_{5/2}$ | 566 | 121.025 | 541.762 | 0.058 | 2.055 | 4.144 |
| Sm₂O₃ (0.04) | | | | | | |
| ${}^4G_{5/2} \rightarrow$ | | | | | | |
| ${}^6H_{11/2}$ | 710 | 373.830 | 545.424 | 0.241 | 1.406 | 1.588 |
| ${}^6H_{9/2}$ | 647 | 521.607 | 735.409 | 0.326 | 1.038 | 1.285 |
| ${}^6H_{7/2}$ | 604 | 150.798 | 841.946 | 0.369 | 2.382 | 4.853 |
| ${}^6H_{5/2}$ | 566 | 149.612 | 321.632 | 0.062 | 1.343 | 1.497 |
| Sm₂O₃ (0.05) | | | | | | |
| ${}^4G_{5/2} \rightarrow$ | | | | | | |
| ${}^6H_{11/2}$ | 710 | 472.025 | 768.693 | 0.242 | 2.253 | 2.716 |
| ${}^6H_{9/2}$ | 647 | 659.147 | 103.643 | 0.327 | 1.182 | 2.133 |
| ${}^6H_{7/2}$ | 604 | 664.422 | 768.927 | 0.373 | 2.403 | 2.824 |
| ${}^6H_{5/2}$ | 566 | 159.127 | 651.741 | 0.056 | 2.237 | 2.388 |

branching ratio holds significant importance for laser designers as it indicates the potential for achieving stimulated emission from a specific transition (Yu et al. 2023). To prevent distortion of the medium in which the rare-earth (RE) ions are arranged, the examination of gain bandwidth ($\sigma_p \times \lambda_{eff}$) and optical gain ($\sigma_p \times \tau$) is crucial. According to Li et al. (2019), a stronger optical amplifier would display larger values of ($\sigma_p \times \lambda_{eff}$) and ($\sigma_p \times \tau$). Notably, the values of ($\sigma_p \times \lambda_{eff}$) and ($\sigma_p \times \tau$) are higher in the ${}^4G_{5/2} \rightarrow {}^6H_{11/2}$ and ${}^6H_{7/2}$ transitions, suggesting that the glasses are well-suited for high-gain laser applications (Li et al. 2019).

7 Conclusion

Zinc tellurite glasses doped with Sm^{3+} ions were produced using the chemical formula of $[(\text{TeO}_2)_{0.7}(\text{ZnO})_{0.3}]_{1-x}[\text{Sm}_2\text{O}_3]_x$ with molar fractions of $x=0.01, 0.02, 0.03, 0.04,$ and 0.05 obtained through the melt quenching method. XRD data confirmed the amorphous nature of the materials. Increasing the Sm_2O_3 content led to higher density and molar volume, attributed to modifications in coordination, structural softening/compactness, and interstitial space of the glass system. Elastic properties investigated revealed unstable patterns in longitudinal and shear velocities, likely due to the formation of non-bridging oxygen's (NBOs) and disruption of the glass network. The ultrasonic velocities decrease from 3392 to 3379 ms^{-1} and 1946 to 1920 ms^{-1} , for V_L and V_S , respectively. Theoretical elastic models have good agreement with the experimental elastic measurements, validating their application. Judd-Ofelt (J-O) intensity parameters indicated higher asymmetry and spectroscopic properties in the synthesized glasses. The glasses exhibited visible emission bands, with the ${}^4\text{G}_{5/2} \rightarrow {}^6\text{H}_{7/2}$ transition showing the most intense emission. The evaluated asymmetry ratios for the transitions ${}^4\text{G}_{5/2} \rightarrow {}^6\text{H}_{9/2}$ and ${}^4\text{G}_{5/2} \rightarrow {}^6\text{H}_{5/2}$ decrease from 4.820 to 0.651 with the electric dipole (ED) transition dominates the magnetic dipole (MD) transition. This suggests low asymmetry present in the sites occupied by Sm^{3+} ions within the glass. The glasses with 0.01 molar percentage of Sm^{3+} showed potential as laser-active media at 604 nm wavelength. These glasses demonstrated higher gain bandwidths, optical gains, branching ratios, and radiative transition probabilities, making them suitable for visible lasers in the strong orange (604 nm) region.

Acknowledgements This study was supported by the Malaysian Ministry of Education (MOE) through the Fundamental Research Grant Scheme (FRGS/1/2018/STG07/UPM/02/12). We would also like to thank the Tertiary Education Trust Fund Nigeria (TETFUND) and the Nigerian Defence Academy Afaka Kaduna in Kaduna State, Nigeria for their valuable support.

Author contribution Tafida Rabi Abubakar: Conceptualization; Investigation; Data curation; Writing and original draft. Seema Thakur: Data curation and validation. Muhammad Yusuf Onimisi: Funding acquisition and supervision. Saidu Garba: Writing-review and editing. Sulaiman Bashir Adamu: Data curation and investigation. Ibrahim Garba Shitu: Data curation and supervision. Ibrahim Ismail Lakin: Validation, Software and visualization.

Funding Universiti Putra Malaysia (FRGS/1/2018/STG07/UPM/02/12, FRGS/1/2018/STG07/UPM/02/12, FRGS/1/2018/STG07/UPM/02/12, FRGS/1/2018/STG07/UPM/02/12, FRGS/1/2018/STG07/UPM/02/12).

Data availability All data presented in the research were generated from various laboratories at Universiti Putra Malaysia, with instruments used for the generation duly acknowledged in the experimental details.

Declarations

Conflict of interest The authors declare that they have no conflict of interest. All results are presented as they appeared and no data was fabricated. Every reference to related works has been carefully acknowledged and cited accordingly in the bibliography. All authors to the work have given consent to be acknowledged for their participation in the research work.

References

- Abd Elfadeel, G., Saddeek, Y.B., Mohamed, G.Y., Mostafa, A.M.A., Shokry-Hassan, H.: Effect of cement kiln dust and gamma irradiation on the ultrasonic parameters of HMO borate glasses. *Nucl. Instrum. Methods Phys. Res. Sect. B Beam Interact. Mater. Atoms* **394**, 44–49 (2017)

- Ahmadi, F., Hussin, R., Ghoshal, S.K.: Spectroscopic attributes of Sm³⁺ doped magnesium zinc sulphosphate glass: Effects of silver nanoparticles inclusion. *Opt. Mater. (Amst)* **73**, 268–276 (2017)
- Alazoumi, S.H., Sidek, H.A.A., Halimah, M.K., Matori, K.A., Zaid, M.H.M., Abdulbaset, A.A.: Synthesis and elastic properties of ternary ZnO–PbO–TeO₂ glasses. *Chalcogenide Lett.* **14**(8), 303–320 (2017)
- Ashur, Z., Mahraz, S., Sahar, M., Ghoshal, S.: Band gap and polarizability of boro-tellurite glass: influence of erbium ions. *J. Mol. Struct.* **1072**, 238–241 (2014)
- Awasthi, K., Srivastava, A., Srivastava, O.N.: Synthesis of carbon nanotubes. *J. Nanosci. Nanotechnol.* **5**(10), 1616–1636 (2005)
- Azlan, M.N., Halimah, M.K., Sidek, H.A.A.: Linear and nonlinear optical properties of erbium doped zinc borotellurite glass system. *J. Lumin.* **181**, 400–406 (2017a)
- Azlan, M.N., Halimah, M.K., El-Mallawany, R., Faznny, M.F., Eevon, C.: Optical properties of zinc borotellurite glass system doped with erbium and erbium nanoparticles for photonic applications. *J. Mater. Sci. Mater. Electron.* **28**(5), 4318–4327 (2017b)
- Bahari, P.H., Sidek, H., Reza, Z.: Ultrasonic and optical properties and emission of Er³⁺/Yb³⁺ doped lead Bismuth-Germanate glass affected by Bi³⁺/Bi²⁺ ions. *J. Lumin.* **143**, 526–533 (2013)
- Bhatia, B., Meena, S.L., Parihar, V., Poonia, M.: Optical basicity and polarizability of Nd³⁺-doped bismuth borate glasses. *New J. Glass Ceram.* **5**, 44–52 (2015)
- Bootjomchai, C.: Comparative studies between theoretical and experimental of elastic properties and irradiation effects of soda lime glasses doped with neodymium oxide. *Radiat. Phys. Chem.* **110**, 96–104 (2015)
- Desirena, H.: Red, green, blue and white light upconversion emission in Yb³⁺/Tm³⁺/Ho³⁺ co-doped tellurite glasses. *J. Phys. D Appl. Phys.* **44**(45), 455308 (2011)
- Eevon, C., Halimah, M.K., Azmi, Z., Azurahaman, C.: Non-destructive ultrasonic technique. *Chalcogenide Lett* **13**(6), 281–289 (2016)
- Elkhoshkhany, N., Abbas, R., Gaafar, M.S., El-Mallawany, R.: Elastic properties of quaternary TeO₂–ZnO–Nb₂O₅–Gd₂O₃ glasses. *Ceram. Int.* **41**(8), 9862–9866 (2015)
- El-Mallawany, R.: Tellurite glasses part I. Elastic properties. *Mater. Chem. Phys.* **53**(97), 93–120 (1998)
- El-Mallawany, R., Abd El-Moneim, A.: Comparison between the elastic moduli of tellurite and phosphate glasses. *Phys. Status Solidi Appl. Res.* **166**(2), 829–834 (1998)
- Gaafar, M.S., Abdeen, M.A.M., Marzouk, S.Y.: Structural investigation and simulation of acoustic properties of some tellurite glasses using artificial intelligence technique. *J. Alloys Compd.* **509**(8), 3566–3575 (2011)
- Gaafar, M.S., Shaarany, I., Alharbi, T.: Structural investigations on some cadmium-borotellurate glasses using ultrasonic, FT-IR and X-ray techniques. *J. Alloys Compd.* **616**, 625–632 (2014)
- Gupta, G., et al.: Influence of bismuth on structural, elastic and spectroscopic properties of Nd³⁺ doped Zinc–Boro–Bismuthate glasses. *J. Lumin.* **149**, 163–169 (2014)
- Hajer, S.S., Halimah, M.K., Azmi, Z., Azlan, M.N.: Optical properties of zinc-borotellurite doped samarium. *Chalcogenide Lett.* **11**(11), 553–566 (2014)
- Hajer, S.S., Halimah, M.K., Azmi, Z., Azlan, M.N.: Effect of samarium nanoparticles on optical properties of zinc Borotellurite glass system. *Mater. Sci. Forum* **846**, 63–68 (2016)
- Halimah, M., et al.: Ultrasonic study and physical properties of borotellurite glasses. *Am. J. Appl. Sci.* **2**(11), 1541–1546 (2005)
- Halimah, M.K., Daud, W.M., Sidek, H.A.: Elastic properties of TeO₂–B₂O₃–Ag₂O glasses. *Ionics (Kiel)* **16**(9), 807–813 (2010)
- Halimah, M.K., Tafida, R.A., Chan, K.T., Muhammad, F.D.: A comparative study of the experimental and the theoretical elastic data of silver oxide incorporated zinc tellurite glass system doped with Sm³⁺ Nps ions. *Optik (Stuttg)* **238**, 166536 (2021)
- Hamza, A.M., et al.: Structural, optical and thermal properties of Er³⁺–Ag codoped bio-silicate borotellurite glass. *Results Phys.* **14**, 102457 (2019a)
- Hamza, A.M., Halimah, M.K., Muhammad, F.D., Chan, K.T.: Physical properties, ligand field and Judd-Ofelt intensity parameters of bio-silicate borotellurite glass system doped with erbium oxide. *J. Lumin.* **207**, 497–506 (2019b)
- Hasnimulyati, L., Halimah, M.K., Zakaria, A., Halim, S.A., Ishak, M.: A comparative study of the experimental and the theoretical elastic data of Tm³⁺ doped zinc borotellurite glass. *Mater. Chem. Phys.* **192**, 228–234 (2017)
- Hua, Y., Li, F., Hu, N., Fu, S.: Frictional characteristics of graphene oxide-modified continuous glass fiber reinforced epoxy composite. *Compos. Sci. Technol.* **223**, 109446 (2022). <https://doi.org/10.1016/j.compscitech.2022.109446>

- Kannappan, R., Thirumaran, A., Palani, S.: Elastic and mechanical properties of glass specimen by ultrasonic method. *J. Eng. Appl. Sci.* **1**(9), 27–31 (2009)
- Li, Y., Hussain, S., Amjad, R.J., Walsh, B.M., Mehmood, H., Akbar, N., Alvi, F., Reza-Dousti, M., Sattar, A., Iqbal, A., Hussain, S.: Calculation of Judd-Ofelt parameters: Sm^{3+} ions doped in zinc magnesium phosphate glasses. *Solid State Commun.* **298**, 113632 (2019)
- Lim, K., Vijaya, N., Kesavulu, C.R., Jayasankar, C.K.: Structural and luminescence properties of Sm^{3+} ions in zinc fluorophosphate glasses. *Opt. Mater. (Amst)* **35**(8), 1557–1563 (2013)
- Linda, D., et al.: Optical properties of tellurite glasses elaborated within the $\text{TeO}_2\text{--Ti}_2\text{O--Ag}_2\text{O}$ and $\text{TeO}_2\text{--ZnO--Ag}_2\text{O}$ ternary systems. *J. Alloys Compd.* **561**, 151–160 (2013)
- Maheshvaran, K., Linganna, K., Marimuthu, K.: Composition dependent structural and optical properties of Sm^{3+} doped boro-tellurite glasses. *J. Lumin.* **131**(12), 2746–2753 (2011)
- Maheshvaran, K., Veeran, P.K., Marimuthu, K.: Optical studies on Eu^{3+} doped Boro-Tellurite glasses. *Solid State Sci.* **1447**(1), 549–550 (2012)
- Makishima, J.D., Mackenzie, A.: Calculation of bulk modulus, shear modulus and Poisson's ratio of glass. *J. Noncryst. Solids* **2**(17), 147–157 (1975)
- Mawlood, S.Q., Ameen, M.M., Sahar, R., Ashur, Z., Mahraz, S., Ahmed, K.F.: Spectroscopic properties of Sm^{3+} doped sodium-tellurite glasses : Judd-Ofelt analysis. *Opt. Mater. (Amst)* **69**, 318–327 (2017)
- Mohamed, N.B., Yahya, A.K., Deni, M.S.M., Mohamed, S.N., Halimah, M.K., Sidek, H.A.A.: Effects of concurrent TeO_2 reduction and ZnO addition on elastic and structural properties of $(90_{-x})\text{TeO}_{2-10}\text{Nb}_2\text{O}_{5-(x)}\text{ZnO}$ glass. *J. Noncryst. Solids* **356**, 1626–1630 (2010)
- Nazrin, I.Z.S.N., Halimah, M.K., Muhammad, F.D., Yip, J.S., Hashimulyati, L., Faznny, M.F., Hazlin, M.A.: The effect of erbium oxide in physical and structural properties of zinc tellurite glass system. *J. Noncryst. Solids* **490**, 35–43 (2018)
- Rao, Y.R., Goud, K.K., Kumar, E.R., Reddy, M.C.S., Rao, B.A.: Upconversion luminescence in $\text{Er}^{3+}/\text{Yb}^{3+}$ codoped lead bismuth indium borate glasses. *Int. J. Recent Dev. Eng. Technol.* **3**(1), 122–130 (2014)
- Saddeek, Y.B.: Ultrasonic study and physical properties of some borate glasses. *Mater. Chem. Phys.* **83**, 222–228 (2004)
- Saddeek, Y.B., Azooz, M.A., Kenawy, S.: Constants of elasticity of $\text{Li}_2\text{O--B}_2\text{O}_3\text{--flyash}$: structural study by ultrasonic technique. *Mater. Chem. Phys.* **94**, 213–220 (2005)
- Seshadri, M., Radha, M., Rajesh, D., Barbosa, L.C., Cordeiro, C.M.B., Ratnakaram, Y.C.: Effect of ZnO on spectroscopic properties of Sm^{3+} doped zinc phosphate glasses. *Phys. B Phys. Condens. Matter* **459**, 79–87 (2015)
- Sidek, H.A.A., et al.: Quantitative analysis on the elastic behaviour of borotellurite glass. *J. Wuhan Univ. Technol. Sci. Ed.* **12**, 863–867 (2007)
- Sidkey, M.A., Gaafar, M.S.: Ultrasonic studies on network structure of ternary $\text{TeO}_2\text{--WO}_3\text{--K}_2\text{O}$ glass system. *Phys. B Condens. Matter* **348**(1–4), 46–55 (2004)
- Sun, L., Liang, T., Sun, X., Li, C., Zhang, C.: Temperature self-compensating and high-sensitivity FBG inclination sensor based on the sliding mass principle. *Opt. Fiber Technol.* **81**, 103539 (2023). <https://doi.org/10.1016/j.yofte.2023.103539>
- Tafida, R.A., et al.: Structural, optical and elastic properties of silver oxide incorporated zinc tellurite glass system doped with Sm^{3+} ions. *Mater. Chem. Phys.* **246**, 122801 (2020)
- Tafida, R.A., Halimah, M.K., Azlan, M.N., Adamu, S.B., Lakin, I.I.: Structural, optical and Judd-Ofelt intensity parameters of samarium doped with zinc tellurite glasses. *Optik (Stuttg)* **262**, 169370 (2022)
- Tafida, R.A., Thakur, S., Onimisi, M.Y., Adamu, S.B., Lakin, I.I.: Samarium nanoparticle-doped silver oxide-incorporated zinc tellurite glass system: structural, elastic, and Judd-Ofelt intensity parameters. *Mater. Chem. Phys.* **296**, 127319 (2023)
- Tanko, Y.A., Ghoshal, S.K., Sahar, M.R.: Ligand field and Judd-Ofelt intensity parameters of samarium doped tellurite glass. *J. Mol. Struct.* **1117**, 64–68 (2016a)
- Tanko, Y.A., Sahar, M.R., Ghoshal, S.K.: Prominent spectral features of Sm^{3+} ion in disordered zinc tellurite glass. *Results Phys.* **6**, 7–11 (2016b)
- Tio, V.O., El-mallawany, R., El-khoshkhany, N., Affi, H.: Ultrasonic studies of $(\text{TeO}_2)_{50}\text{--}(\text{V}_2\text{O}_5)_{50-x}\text{--}(\text{TiO}_2)_x$ glasses. *Mater. Chem. Phys.* **95**, 321–327 (2006)
- Umar, S.A., Halimah, M.K., Chan, K.T., Latif, A.A.: Physical, structural and optical properties of erbium doped rice husk silicate borotellurite (Er-doped RHSBT) glasses. *J. Noncryst. Solids* **472**, 31–38 (2017)
- Usman, A., Halimah, M.K., Latif, A.A., Muhammad, F.D., Abubakar, A.I.: Influence of Ho^{3+} ions on structural and optical properties of zinc borotellurite glass system. *J. Noncryst. Solids* **483**, 18–25 (2018)
- Yu, X., Mao, L., Xie, H., Yao, X., He, G., Huang, Z.: Flotation behavior and adsorption mechanism of phenylpropyl hydroxamic acid as collector agent in separation of fluorite from calcite. *Langmuir* **39**(16), 5936–5943 (2023). <https://doi.org/10.1021/acs.langmuir.3c00584>

- Zaid, B.Z.A.M.H.M., Matori, K.A., Wah, L.C., Sidek, H.A.A., Halimah, M.K., Wahab, Z.A.: Elastic moduli prediction and correlation in soda lime silicate glasses containing ZnO. *Int. J. Phys. Sci.* **6**(6), 1404–1410 (2011)
- Zaitizila, I., Halimah, M., Muhammad, F.D., Nurisya, M.: Influence of manganese doping on elastic and structural properties of silica borotellurite glass. *J. Noncryst. Solids* **492**, 50–55 (2018)

Publisher's Note Springer Nature remains neutral with regard to jurisdictional claims in published maps and institutional affiliations.

Springer Nature or its licensor (e.g. a society or other partner) holds exclusive rights to this article under a publishing agreement with the author(s) or other rightsholder(s); author self-archiving of the accepted manuscript version of this article is solely governed by the terms of such publishing agreement and applicable law.

Authors and Affiliations

R. A. Tafida^{1,2} · S. Thakur³ · M. Y. Onimisi¹ · S. Garba¹ · S. B. Adamu^{2,4} · I. G. Shitu^{2,4} · I. I. Lakin^{2,5}

✉ R. A. Tafida
tafidajalingo@yahoo.com

¹ Department of Physics, Nigerian Defence Academy, Afaka, PMB 2109, Kaduna, Kaduna State, Nigeria

² Department of Physics, Faculty of Science, University Putra Malaysia, UPM, 43400 Serdang, Selangor, Malaysia

³ Department of Humanity and Science, A.C. Patil College of Engineering, Kharghar, Navi Mumbai, Maharashtra 410210, India

⁴ Department of Physics, Sule Lamido University, Kafin Hausa, Jigawa State, Nigeria

⁵ Physics Department, Kaduna State University, Kaduna, Nigeria